Unified Reaction Valley Approach Mechanism of the Reaction $CH_3 + H_2 \rightarrow CH_4 + H$

Zoran Konkoli, Elfi Kraka,* and Dieter Cremer

Department of Theoretical Chemistry, University of Göteborg, Kemigården 3, S-41296 Göteborg, Sweden

Received: September 19, 1996; In Final Form: December 18, 1996[⊗]

A unified reaction valley analysis (URVA) is presented to investigate the mechanism of the reaction $CH_3 + H_2 \rightarrow CH_4 + H$ at the UMP2/6-31G(d,p) level of theory. URVA is based on the reaction path Hamiltonian, the intrinsic reaction coordinate s, and the characterization of normal modes $\omega_\mu(s)$, reaction path vector $\boldsymbol{\eta}(s)$, and curvature vector $\kappa(s)$ in terms of generalized adiabatic modes $\mathbf{a}_n^g(s)$ associated with internal parameters that are used to describe the reaction complex. In addition, URVA combines the investigation of the harmonic reaction valley with the analysis of attractive and repulsive forces exerted on the nuclei by analyzing the electron density distribution $\rho(\mathbf{r},s)$. It is shown that changes in $\rho(\mathbf{r},s)$ reflect changes in the reaction valley and vice versa. Five reaction phases can be distinguished (reactant, reactant preparation, transition state (TS), product preparation, and product phase), of which the chemically relevant phases are indicated by small (reorganization of electron structure) and large curvature peaks (bond breaking or forming). Relatively large peaks of the adiabatic force constants indicate those positions at which the reaction is accelerated by appropriate electronic structure changes. Position and height of the curvature peaks in the TS region reflect the energetics of the reaction and the nature of the TS in the sense of the Hammond postulate: The reaction is exothermic with an early TS that is shifted by $\Delta s = 0.3$ amu$^{1/2}$ a_0 into the entrance channel.

1. Introduction

The investigation of reaction mechanism by theoretical means is normally done by determining energy, geometry, and other properties of reactants, products, and transition state (TS) complex and, then, discussing energetics, geometry changes, and electronic structure changes by focusing just on the stationary points of the potential energy surface (PES) along the reaction path. A more detailed analysis of reaction mechanism is possible by using the reaction path Hamiltonian (RPH) introduced by Miller, Handy, and Adams[1] and investigating the reaction valley that connects the stationary points associated with reactants, TS, and products. In this approach, the $(3K - L)$-dimensional space (L, number of rotations and translations), in which the reaction of a molecular system with K atoms is described, is partitioned into a one-dimensional reaction path space along which the translational motion of the reaction system takes place and a $((3K - L) - 1)$-dimensional orthogonal space, in which the transverse vibrations of the reaction system orthogonal to the reaction path movement occur. In other words, one distinguishes between the path along the valley floor and the shape of the valley in the transverse directions when following the reaction path from reactants to products.

Essential for the investigation of reaction path and reaction valley are the intrinsic reaction coordinates (IRCs),[2] the direction of the reaction path given by the reaction path vector $\boldsymbol{\eta}(s)$ (Scheme 1), the curvature of the reaction path given by the curvature vector $\kappa(s)$ (Scheme 1)[3] and the curvature of the valley orthogonal to the reaction path given by the force constants associated with the generalized normal modes $\mathbf{l}_\mu^g(s)$.[1] The exchange of energy between reaction path mode and transverse vibrational modes can be studied by these quantities as has been demonstrated in many investigations.[1−6]

In this work, we present a new way of investigating the reaction valley based on the RPH of Miller, Handy, and Adams[1] and the generalization of the adiabatic mode concept introduced by Konkoli and Cremer.[7−10] In addition, we analyze the forces exerted on the atoms of the reaction system along the reaction path with the help of the electron density distribution $\rho(\mathbf{r},s)$. Changes in $\rho(\mathbf{r},s)$ reflect electronic structure changes, which can directly be related to properties of the PES along the reaction path as they are given by gradient (forces on the atoms) and Hessian (force constants). The electron density distribution $\rho(\mathbf{r},s)$ determines all changes in the geometry of the reaction complex along the reaction path, which are reflected by its direction $\boldsymbol{\eta}(s)$ and its curvature vector $\kappa(s)$. Hence, the simultaneous analysis of energy, geometry, electron density distribution, translational mode along s, and transverse vibrational modes leads to a new way of investigating the reaction valley and the mechanism of the chemical reaction that can take place by following the reaction valley from reactants to products. Since this new approach combines several tools previously applied in separate studies of chemical reactions or just equilibrium structures, we have coined for it the term *unified reaction valley analysis* (URVA). The URVA approach represents a *direct method* because all needed calculations and the analysis of results are done in one step once reactants, products, and TS are known.

SCHEME 1

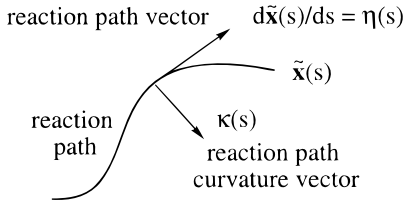

In this work, we present the theory of URVA and then discuss its application to the hydrogenation reaction of the methyl radical:

$$CH_3(^2A_2'') + H_2(^1\Sigma_g^+) \rightarrow CH_4(^1A_1) + H(^2S) \qquad (I)$$

Reaction I has been extensively studied both by experimental[11] and theoretical means.[12−20] Kraka and co-workers[12]

[⊗] Abstract published in *Advance ACS Abstracts,* February 1, 1997.

S1089-5639(96)02877-0 CCC: $14.00

presented the most accurate ab initio description of the energetics of reaction I using CCSD(T) in connection with VQZ+3P basis sets. The dynamics of the reaction was investigated by Yamashita and Yamabe[13] at the UHF/4-31G level, by Boatz and Gordon[15] as well as Baldrige and co-workers[16] at the UHF/STO-3G level of theory, by Truong at QCISD/6-311G(d,p),[17] by Truong and Duncan at DFT/6-311G(d,p),[18] and by Taketsugu and Gordon at CASSCF(9,9)/6-31G(d,p),[19] all of them using the RPH. Other investigations of reaction I utilized besides ab initio also semiempirical or empirical information on the PES.[20] All investigations concentrated on the TS region, typically varying the reaction coordinate s between ± 2 amu$^{1/2}$ a_0. Because of cost reasons or computational difficulties, none of the previous investigations included regions of s, for which van der Waals interactions can be expected and in which the course of the reaction may be determined. We will show in the present work that the investigation of the van der Waals region is indeed of importance to understand the mechanism of reaction I.

2. Theory

Since the theory of the RPH has amply been documented in the literature,[1,3,5] here just some necessary definitions are given.

The reaction path used in the RPH approach is the steepest descent path in mass-weighted coordinates.[1] It is defined by the line $\tilde{\mathbf{x}}(s)$, where $\tilde{\mathbf{x}}(s)$ is a column vector with $3K$ mass-weighted Cartesian coordinates $\mathbf{x}_i$. In this and the following the tilde indicates mass weighting. The reaction path is given parametrically in terms of its arc length s defined by the differential

$$ds^2 = d\mathbf{x}^+ \mathbf{M}\, d\mathbf{x} = d\tilde{\mathbf{x}}^+ d\tilde{\mathbf{x}} \tag{1}$$

with $\mathbf{M}$ being the diagonal matrix of nuclear masses. The direction of the reaction path $\tilde{\mathbf{x}}(s)$ is determined by eq 2

$$\mathbf{M}\frac{d\mathbf{x}(s)}{ds} = -\frac{\mathbf{g}(\mathbf{x}(s))}{c(s)} \tag{2a}$$

$$\frac{d\tilde{\mathbf{x}}(s)}{ds} = \mathbf{M}^{1/2}\frac{d\mathbf{x}(s)}{ds} = -\mathbf{M}^{-1/2}\frac{\mathbf{g}(\mathbf{x}(s))}{c(s)} = -\frac{\tilde{\mathbf{g}}(\tilde{\mathbf{x}}(s))}{c(s)} = \boldsymbol{\eta}(s) \tag{2b}$$

which defines the reaction path vector $\boldsymbol{\eta}(s)$ identical with the normalized energy gradient vector in mass-weighted Cartesian coordinates. The normalization constant $c(s)$ is given by eq 3:[3]

$$c(s) = \sqrt{\mathbf{g}^+(\mathbf{x}(s))\mathbf{M}^{-1}\mathbf{g}(\mathbf{x}(s))} = \sqrt{\tilde{\mathbf{g}}^+(\tilde{\mathbf{x}}(s))\,\tilde{\mathbf{g}}(\tilde{\mathbf{x}}(s))} \tag{3}$$

To obtain the RPH, $N_{\text{vib}} = (3K - L) - 1$ (nonlinear reaction complexes, $N_{\text{vib}} = 3K - 7$; linear reaction complexes, $N_{\text{vib}} = 3K - 6$) mass-weighted generalized normal modes $\tilde{\mathbf{l}}_\mu^{\,g}(s)$, $\mu = 1, 2, ..., N_{\text{vib}}$ and their associated frequencies $\omega_\mu(s)$ have to be calculated by diagonalizing the mass-weighted projected force constant matrix $\tilde{\mathbf{K}}^g(s)$ given by eq 4[3]

$$\tilde{\mathbf{K}}^g(s)\,\tilde{\mathbf{l}}_\mu^{\,g}(s) = \omega_\mu^{\,2}(s)\,\tilde{\mathbf{l}}_\mu^{\,g}(s) \tag{4}$$

where $\tilde{\mathbf{K}}^g(s)$ is defined by eq 5:

$$\tilde{\mathbf{K}}^g(s) = (\mathbf{I} - \tilde{\mathbf{P}}(s))\tilde{\mathbf{f}}(s)(\mathbf{I} - \tilde{\mathbf{P}}(s)) \tag{5}$$

In eq 5, $\tilde{\mathbf{f}}(s)$ is the mass-weighted Cartesian coordinate force constant matrix and $\mathbf{I} - \tilde{\mathbf{P}}(s)$ is a projector onto the $((3K - L) - 1)$-dimensional subspace of normal mode vibrations orthogonal to the reaction path mode.[1,3] After generalized normal modes have been found, a "harmonic" reaction valley is described according to eq 6

$$V(s,\boldsymbol{Q}) = V(s) = \frac{1}{2}\sum_{\mu=1}^{N_{\text{vib}}} k_\mu^{\,g}(s)\,[Q_\mu^{\,g}(s)]^2 \tag{6}$$

where $k_\mu^g(s)$ is the generalized normal mode force constant, $Q_\mu^g(s)$ the generalized normal mode coordinate, and $V(s)$ the energy profile along the reaction path.

To describe energy transfer along the reaction path, curvature vector $\boldsymbol{\kappa}(s)$, curvature coupling elements $B_{\mu,s}(s)$, and mode-mode coupling elements $B_{\mu,\nu}(s)$ have to be calculated.[3] The mass-weighted curvature vector $\tilde{\boldsymbol{\kappa}}(s)$ is defined by eq 7a and its Euclidean norm by eq 7b.

$$\tilde{\boldsymbol{\kappa}}(s) = \frac{d^2\tilde{\mathbf{x}}(s)}{ds^2} \tag{7a}$$

$$\kappa(s) = \sqrt{\tilde{\boldsymbol{\kappa}}(s)^+\,\tilde{\boldsymbol{\kappa}}(s)} \tag{7b}$$

By differentiation of eq 2, one obtains eq 8.

$$\boldsymbol{\kappa}(s) = \frac{1}{\tilde{c}(s)}\left(\tilde{\mathbf{f}}(s)\frac{\tilde{\mathbf{g}}(s)}{\tilde{c}(s)} - \left(\left(\frac{\tilde{\mathbf{g}}(s)}{\tilde{c}(s)}\right)^+\tilde{\mathbf{f}}(s)\frac{\tilde{\mathbf{g}}(s)}{\tilde{c}(s)}\right)\frac{\tilde{\mathbf{g}}(s)}{\tilde{c}(s)}\right) \tag{8}$$

The curvature coupling elements $B_{\mu,s}(s)$, which represent coefficients of the expansion of the curvature vector in terms of generalized normal modes $\tilde{\mathbf{l}}_\mu^{\,g}(s)$, are defined by eq 9:

$$B_{\mu,s}(s) = \tilde{\boldsymbol{\kappa}}(s)^+\,\tilde{\mathbf{l}}_\mu^{\,g}(s) \tag{9}$$

Mode−mode coupling elements $B_{\mu,\nu}(s)$ are given by eq 10:

$$B_{\mu,\nu}(s) = \tilde{\mathbf{l}}_\mu^{\,g+}(s)\frac{d\tilde{\mathbf{l}}_\nu^{\,g}}{ds} \tag{10}$$

Combining eq 10 with eq 4 leads to eq 11 for the mode−mode coupling elements

$$B_{\mu,\nu}(s) = \frac{\tilde{\mathbf{l}}_\mu^{\,g+}(s)\frac{d\tilde{\mathbf{K}}^g(s)}{ds}\tilde{\mathbf{l}}_\nu^{\,g}(s)}{\omega_\nu^{\,2} - \omega_\mu^{\,2}} \tag{11}$$

The derivative of $\tilde{\mathbf{K}}^g(s)$ can be calculated according to eq 12

$$\frac{d\tilde{\mathbf{K}}^g(s)}{ds} = -\frac{d}{ds}\tilde{\mathbf{P}}(s)\,\tilde{\mathbf{f}}(s)(\mathbf{I} - \tilde{\mathbf{P}}(s)) - (\mathbf{I} - \tilde{\mathbf{P}}(s))\tilde{\mathbf{f}}(s)\frac{d}{ds}\tilde{\mathbf{P}}(s) + (\mathbf{I} - \tilde{\mathbf{P}}(s))\frac{d}{ds}\tilde{\mathbf{f}}(s)(\mathbf{I} - \tilde{\mathbf{P}}(s)) \tag{12}$$

where the derivative of the projector $\tilde{\mathbf{P}}(s)$ has been given by Page and McIver.[3]

It has become a common practice to graphically present the norm of the curvature vector, $\kappa(s)$, and to discuss energy transfer along the reaction path in terms of the maxima of $\kappa(s)$.[4] Maximal values of $\kappa(s)$ indicate those points on the path where energy can flow from the motion along the reaction path into one of the transverse normal vibrational modes or vice versa thus decreasing or increasing the reaction rate. The curvature coupling coefficients $B_{\mu,s}(s)$ of eq 9 determine how much energy is transferred into (retrieved from) normal mode $\tilde{\mathbf{l}}_\mu^{\,g}(s)$. Due to the delocalized character of normal modes, it is difficult to identify substituents or molecular fragments, which by their vibrations are predominantly responsible for energy transfer from the reaction path mode into vibrational modes (rate reduction) or alternatively can be used to channel external energy

via vibrational modes into the reaction path mode (rate enhancement). Therefore, it is desirable to express the curvature coupling coefficients $B_{\mu,s}(s)$ of eq 9 in terms of vibrational modes that can be directly associated with chemically relevant molecular fragments or structural units. Such modes are the adiabatic internal modes $\mathbf{a}_n$, which have recently been suggested for the analysis of vibrational spectra of molecules in their equilibrium geometry.[7] In the following, we will present a generalization of these internal modes for use in connection with the RPH.

2.1 Construction of Generalized Adiabatic Modes $\mathbf{a}_n^g(s)$. Adiabatic internal vibrational modes described by the mode vector $\mathbf{a}_n$ are elementary vibrational modes associated with an internal parameter ζ_n used to describe molecular fragment ϕ_n.[7−10] For example, $\mathbf{a}_n$ can be the vector of a stretching mode associated with the bond length r(AB) of a diatomic fragment ϕ(AB) within a molecule. The adiabatic modes are based on a dynamic principle (leading parameter principle[7]) and are directly obtained from a modified form of the Euler−Lagrange equations.[7] They comply with the symmetry of the molecule and are independent of the choice of the set of internal parameters ζ_n. Furthermore, they are perfectly suited to characterize normal vibrational modes (characterization of normal modes (CNM) approach)[9,10] in the common language of chemistry that attempts to express molecular properties in form of internal parameters ζ_n such as internal coordinates q_n.

In this work, (localized) internal coordinates q_n are used as internal parameters since chemists are familiar with these coordinates. However, internal coordinates q_n represent just one possible choice of internal parameters ζ_n, which in principle could be linear combinations of internal coordinates often used to describe rocking, wagging, or torsion of functional groups (e.g. symmetry-adapted internal coordinates, natural coordinates,[21] puckering coordinates,[22] or any other choice of suitable coordinates). Therefore, in the following we will continue to speak of internal parameters even though just internal coordinates are used.

In this work, we extend the procedure previously described for constructing adiabatic modes at equilibrium points of the PES to points along a reaction path by requiring that the harmonic part of the energy in eq 6 has to be minimized with regard to displacements in the $((3K - L) - 1)$-dimensional vibrational space (rather than the $(3K - L)$-dimensional space as originally defined[7]) while relaxing all internal parameters but one. The internal parameter, which is kept frozen, is called the leading parameter ζ_n.[7]

Equation 13 gives the conditions for obtaining generalized adiabatic internal modes $\mathbf{a}_n^g(s)$:

$$V(\mathbf{Q},s) = \min \tag{13a}$$

$$s = \text{const} \tag{13b}$$

$$\zeta_n(s,\mathbf{Q}) = \zeta_n^* \tag{13c}$$

where in first order the leading parameter ζ_n is some linear function of the normal mode coordinates, i.e. in the limit of infinitesimal displacements it is defined by eq 14:

$$\zeta_n(s,\mathbf{Q}) = \sum_{\mu=1}^{N_{vib}} D_{n\mu}(s)\, Q_\mu(s) \tag{14}$$

$D_{n\mu}(s)$ denotes an element of a Wilson B-type matrix $\mathbf{D}$ that connects normal coordinates with internal coordinates. Solving eq 13, generalized adiabatic internal modes and related force constants $k_n^a(s)$, mass $m_n^a(s)$, and frequency $\omega_n^a(s)$ are obtained by eqs 15[7]

$$(\mathbf{a}_n(s))_\mu = \frac{\dfrac{D_{n\mu}(s)}{k_\mu^{\,g}(s)}}{\displaystyle\sum_{\nu=1}^{N_{vib}} \frac{D_{n\nu}(s)^2}{k_\nu^{\,g}(s)}} \tag{15a}$$

$$k_n^{\,a}(s) = \frac{1}{\displaystyle\sum_{\nu=1}^{N_{vib}} \frac{D_{n\nu}(s)^2}{k_\nu^{\,g}(s)}} \tag{15b}$$

$$m_n^{\,a}(s) = \frac{1}{G_{nn}(s)} \tag{15c}$$

$$\omega_n^{\,a}(s) = \sqrt{\frac{k_n^{\,a}(s)}{m_n^{\,a}(s)}} \tag{15d}$$

where $G_{nn}(s)$ is an element of the Wilson $\mathbf{G}$ matrix. Generalized adiabatic modes can be transformed from normal mode space into Cartesian coordinate space according to eq 16

$$(\mathbf{a}_n^{\,g}(s))_i = \sum_{\mu=1}^{N_{vib}} (\mathbf{l}_\mu(s))_i\, (\mathbf{a}_n^{\,g}(s))_\mu \qquad i = 1, ..., 3N \tag{16}$$

where $(\mathbf{l}_\mu)_i$ is component i of normal mode vector $\mathbf{l}_\mu$ in Cartesian coordinates.

Equation 15 indicates that there is no difference in applying the adiabatic mode concept to an equilibrium geometry or to a point along a reaction path. In the latter case, the adiabatic modes are defined in a $((3K - L) - 1)$- rather than a $(3K - L)$-dimensional space and all adiabatic properties are a function of s. Obviously, the adiabatic mode concept and the leading parameter principle have their strength in the fact that they can generally be applied to equilibrium geometries as well as any point on the reaction path. In addition, the extension to points on ridge paths between reaction valleys is straightforward since it implies just another constraint besides eq 13b concerning the direction of the vibrational mode with imaginary frequency.

2.2 Analysis of Curvature Vector and Generalized Normal Modes in Terms of Generalized Adiabatic Modes $\mathbf{a}_n^g(s)$. Once generalized adiabatic modes $\mathbf{a}_n^g(s)$ have been defined, the normal modes and curvature vector can be analyzed utilizing the characterization of normal modes (CNM) approach described previously.[9,10] For this purpose, the amplitude $A_{n,s}$ is defined

$$A_{n,s} = \frac{\kappa(s)^+\, \mathbf{M}(s)\, \mathbf{a}_n^{\,g}(s)}{\sqrt{\mathbf{a}_n^{\,g+}(s)\, \mathbf{M}(s)\, \mathbf{a}_n^{\,g}(s)}} \tag{17}$$

which characterizes the curvature vector $\kappa(s)$ in terms of generalized adiabatic modes associated with internal parameters used to describe the reaction system. It corresponds to the A-type amplitude AvAM (with metric $\mathbf{M}$), which was found to present the best choice for kinetically characterizing normal modes in terms of adiabatic modes in the case of molecules in their equilibrium geometries.[9] Equation 17 ensures that $A_{n,s}$ has the same dimension as $B_{\mu,s}$ and, for $\mathbf{l}_\mu^{\,g} = \mathbf{a}_n^{\,g}$, amplitude $A_{n,s}$ and coefficient $B_{\mu,s}$ are equal. Both curvature vector and normal modes orthogonal to the reaction path are characterized within URPA in terms of generalized adiabatic internal modes; however, for the latter the A-type amplitude AvAF (metric $\mathbf{f}$)

is used since for these modes the dynamic characterization is more important than a kinetic one.

2.3 Analysis of Reaction Path Vector $\boldsymbol{\eta}(s)$. Kato and Morokuma[4] suggested a procedure to analyze the reaction path vector $\boldsymbol{\eta}(s)$ by expressing d**x**/ds in terms of basis vectors $\mathbf{u}_n(s)$

$$\frac{\mathrm{d}\mathbf{x}(s)}{\mathrm{d}s} = \sum_{n=1}^{3K-L} t_n(s)\,\mathbf{u}_n(s) \tag{18}$$

with vectors $\mathbf{u}_n(s)$ being equal to

$$\mathbf{u}_n(s) = \mathbf{M}^{-1}\mathbf{b}_n(s) \tag{19}$$

and $\mathbf{b}_n$ being given by eq 20

$$(\mathbf{b}_n(s))_i = \frac{\partial q_n(\mathbf{x})}{\partial x_i} \tag{20}$$

The coefficients t_n of expansion 18 have been used to characterize the reaction path vector $\boldsymbol{\eta}(s)$. For a nonredundant set of internal coordinates, they are given by eq 21:

$$t_n(s) = (\mathbf{C}^{+}\mathbf{g})_n(s)/c(s) = \gamma_n(s)/c(s) \tag{21}$$

Matrix **C** contains in its columns vectors $\mathbf{c}_n$,[7] and $\gamma_n(s)$ is a component of the gradient being expressed in internal coordinates.

We provide here a basis for using eqs 18−21 by considering the question (a) whether the choice of $\mathbf{u}_n$ as given in eq 19 is the best one and (b) whether it is possible to generalize eq 18 under direct consideration of the definition of the reaction path given by eqs 1 and 2.

It is obvious that basis vectors $\mathbf{u}_n$ cannot be chosen to be the adiabatic internal mode vectors $\mathbf{a}_n{}^{\mathrm{g}}$ since the latter are constructed for the analysis of molecular vibrations in the $((3K - L) - 1)$-dimensional space orthogonal to the reaction path. However, basis vector $\mathbf{u}_n$ should represent an internal mode associated with an internal parameter ζ_n (or as a special case an internal coordinate q_n) and a molecular fragment or structural subunit ϕ_n in the same way as vector $\mathbf{a}_n{}^{\mathrm{g}}$ does, and therefore, the same procedure used for constructing the latter should be applied to get suitable internal vectors $\mathbf{u}_n$.

Extending the leading parameter principle to internal vectors $\mathbf{u}_n$, we require that in view of eq 1 Δs^2 is minimized under the constraint that for any arbitrary change of $\Delta\mathbf{x}$, the change of the internal parameter $\zeta_n(\mathbf{x})$ is equal to a constant $\Delta\zeta_n{}^*$:

$$[\Delta s(\Delta\mathbf{x})]^2 = \frac{1}{2}\Delta\mathbf{x}^{+}\mathbf{M}\Delta\mathbf{x} = \min \tag{22a}$$

$$\Delta\zeta_n(\Delta\mathbf{x}) = \mathbf{b}_n(s)\Delta\mathbf{x} = \Delta\zeta_n{}^* \tag{22b}$$

By using the method of Lagrange multipliers according to eq 23

$$\frac{\partial}{\partial\Delta x_i}\left[\frac{1}{2}\Delta\mathbf{x}^{+}\mathbf{M}\Delta\mathbf{x} - \lambda\mathbf{b}_n(s)\Delta\mathbf{x}\right] = 0 \tag{23}$$

one obtains

$$\Delta\mathbf{x} = \lambda\mathbf{M}^{-1}\mathbf{b}_n \tag{24}$$

By inserting eq 24 into eq 22b, the value of the Lagrange multiplier λ is given by eq 25:

$$\lambda = \frac{\Delta\zeta_n{}^*}{\mathbf{b}_n\mathbf{M}^{-1}\mathbf{b}_n{}^{+}} \tag{25}$$

Since $\Delta\mathbf{x}$ is to be expressed in terms of basis vectors $\mathbf{v}_n$[7]

$$\Delta\mathbf{x} = \mathbf{v}_n\Delta\zeta_n \tag{26}$$

the final form of $\Delta\mathbf{x}$ resulting from eqs 24 and 25

$$\Delta\mathbf{x} = \frac{\mathbf{M}^{-1}\mathbf{b}_n(s)}{\mathbf{b}_n(s)\mathbf{M}^{-1}\mathbf{b}_n{}^{+}(s)}\Delta\zeta_n{}^* \tag{27}$$

reveals that the basis vectors $\mathbf{v}_n$ obtained in this way are identical to the basis vectors $\mathbf{u}_n$ defined in eq 19 apart from a proportionality factor given by the denominator of the left side of eq 27. Hence, vectors $\mathbf{u}_n$ are the internal modes that characterize the movement along the reaction path and, therefore, represent the equivalent to the adiabatic internal modes for analysis of the transverse normal vibrational modes.

Characterization of the Reaction Path Vector. Once the basis vectors $\mathbf{u}_n$ are defined one could think of characterizing the reaction path vector $\boldsymbol{\eta}(s) = \mathrm{d}\mathbf{x}/\mathrm{d}s$ with the help of the PED analysis.[23,24] However, in view of the disadvantages of the PED analysis (dependence on the choice of the set of internal parameters, large frequency uncertainties, symmetry problems) discussed previously,[9,10] we refrain from applying the PED analysis. Instead, we generalize the definition of a parameter set independent amplitude *A* introduced in ref 9 to the case of the reaction path vector

$$A_{n,s} = \frac{\left(\frac{\mathrm{d}\mathbf{x}}{\mathrm{d}s},\mathbf{u}_n\right)^2}{\left(\frac{\mathrm{d}\mathbf{x}}{\mathrm{d}s},\frac{\mathrm{d}\mathbf{x}}{\mathrm{d}s}\right)(\mathbf{u}_n,\mathbf{u}_n)} \tag{28}$$

with

$$(\mathbf{a},\mathbf{b}) = \sum_{i=1}^{3K} a_i O_{ij} b_j \tag{29}$$

which by virtue of eqs 2 and 19 and the metric $\mathbf{O} = \mathbf{M}$ can be rewritten as

$$A_{n,s} = \frac{(\mathbf{g}^{+}\mathbf{M}^{-1}\mathbf{b}_n)^2}{(\mathbf{g}^{+}\mathbf{M}^{-1}\mathbf{g}_n)(\mathbf{b}_n{}^{+}\mathbf{M}^{-1}\mathbf{b}_n)} \tag{30}$$

The definition of the amplitude given by eq 30 considers (besides electronic effects) the kinetic aspect of the translational motion along the reaction path. Alternatively, one can use as a metric the unit matrix **I**, and by this consider just electronic effects, which influence the direction of the reaction path:

$$A_{n,s}{}^{\mathrm{el}} = \frac{(\mathbf{g}^{+}\mathbf{b}_n)^2}{(\mathbf{g}^{+}\mathbf{g}_n)(\mathbf{b}_n{}^{+}\mathbf{b}_n)} \tag{31}$$

Both definitions 30 and 31 (they are related to the amplitudes AvAM and AvAF used for the CNM of vibrational spectra of nonreacting molecules at their equilibrium[9,10]) are useful for the analysis of $\boldsymbol{\eta}(s)$ although amplitude 30 should be given preference. Apart from this, there are other possibilities of defining amplitude $A_{n,s}$ that differ with regard to the choice of internal vibration $\mathbf{u}_n$ or metric **O**. For example, for $\mathbf{u}_n$ one could use $\mathbf{u}_n = \mathbf{c}_n$ (see ref 7 for definition of vectors $\mathbf{c}_n$) and for **O** one could take the force constant matrix in Cartesian coordi-

SCHEME 2

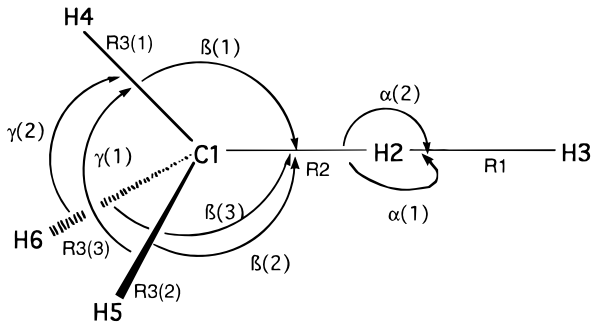

nates, **f**. However, the choice of $\mathbf{u}_n$ and **O** given in eqs 19 and 30 are to be preferred since they are directly connected to the definition of the reaction path vector given in eq 2.

3. Computational Methods

In this work, unrestricted Møller−Plesset perturbation theory at second order (UMP2)[25] is applied using Pople's VDZ+P basis set 6-31G(d,p).[26] As suitable internal parameters ζ_n for describing the reaction complex, the nonredundant set of $3K - 6 = 12$ internal coordinates q_n shown in Scheme 2 was used. The IRC was generated by the method of Gonzales and Schlegel[27] with a step size of 0.05 amu$^{1/2}$ a_0 that was reduced at positions of avoided mode−mode crossings to smaller step sizes.[28] Analytical gradients **g** and force constant matrices **f** were calculated in the region $-3 < s < 3$ amu$^{1/2}$ a_0. For each value of the reaction coordinate s, the reaction path vector $\boldsymbol{\eta}(s)$ and its decomposition in terms of $\mathbf{u}_n$ vectors, the $3K - 7$ generalized normal modes $\mathbf{l}_\mu^g(s)$ with associated frequencies $\omega_\mu^g(s)$, the decomposition of $\mathbf{l}_\mu^g(s)$ in terms of generalized adiabatic internal modes $\mathbf{a}_n^g(s)$, adiabatic force constants $k_n^a(s)$ associated with the internal coordinates given in Scheme 2, reaction path curvature $\kappa(s)$, and coupling coefficients $B_{\mu,s}(s)$ and $B_{\mu,\nu}(s)$ were calculated.

In previous work on reaction I, calculated harmonic normal mode frequencies $\omega_\mu(s)$ were presented in either an adiabatic fashion (see, e.g., refs 17, 18, and 20b,c,g,l) identifying avoided crossings by appropriate symmetry criteria or a diabatic fashion (see, e.g. refs 13, 16, and 20n). We used the DMO program, which automatically handles all avoided crossings in a diabatic fashion and which is described elsewhere.[28] In the case of reaction I, DMO correctly resolved all avoided crossings as will be shown in the following discussion.

The electron density distribution $\rho(\mathbf{r},s)$ of the reaction complex was analyzed by generating along the path contour line diagrams of the difference density distribution $\Delta\rho(\mathbf{r},s)$

$$\Delta\rho(\mathbf{r},s) = \rho(\mathbf{r},s)[\text{reaction complex}] - \rho(\mathbf{r},s)[\text{procomplex}] \quad (32)$$

as well as the Laplace concentrations $-\nabla^2\rho(\mathbf{r},s)$ and the difference Laplace concentration

$$\Delta\nabla^2\rho(\mathbf{r},s) = \nabla^2\rho(\mathbf{r},s)[\text{reaction complex}] - \nabla^2\rho(\mathbf{r},s)[\text{procomplex}] \quad (33)$$

Each difference density distribution was calculated by including basis set superposition corrections according to the counterpoise method.[29] The electron density of the procomplex was defined according to

$$\rho(\mathbf{r},s)[\text{procomplex}] = 0.5\{\rho(\mathbf{r},s)[CH_3] + \rho(\mathbf{r},s)[H_2] + \rho(\mathbf{r},s)[CH_4] + \rho(\mathbf{r},s)[H]\} \quad (34)$$

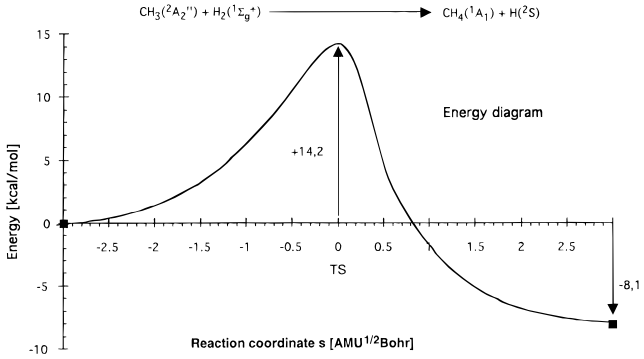

Figure 1. UMP2/6-31G(d,p) energy as a function of the reaction coordinate s for the reaction $CH_3 + H_2 \rightarrow CH_4 + H$. The position of the transition state corresponds to $s = 0$ amu$^{1/2}$ a_0.

where for each molecular subunit the geometry was defined by the geometry it adopts within the reaction complex at point s. Difference density and Laplace concentration were analyzed as outlined previously[30] using throughout this work UMP2/6-31G-(d,p) response densities.

All calculations needed for URVA were carried out with the program ADIA,[31] which is a multipurpose package for the analysis of vibrational spectra and the URVA approach. It contains DMOL and represents a part of the ab initio package COLOGNE.[32] ADIA also prepares the data for later use in form of graphical representations. For the UMP2 calculations, the ab initio package GAUSSIAN94 was used.[33]

4. The Unified Reaction Valley Analysis

The analysis of reaction I is presented in 10 figures, which are automatically generated in the course of a dynamical investigation with the URVA approach. They are grouped into four figures that summarize features of the one-dimensional reaction space (the reaction path following the valley floor) and six figures that summarize features of the $(3K - 7)$-dimensional vibrational space (the harmonic reaction valley).

One-dimensional reaction space:

(1) Energy profile $E(s)$ describes the energetics of the reaction (energy barrier, reaction energy) (Figure 1).

(2) Geometry changes of the reaction complex as a function of s, which describe the geometries of reactants, TS, and products, as well as all intermediate points along s (Figure 2).

(3) Analysis of the reaction path vector $\boldsymbol{\eta}(s)$ considering just electronic effects or electronic and mass effects at the same time (Figure 3a,b).

(4) Analysis of the internal forces as a function of s and identification of s-regions with attraction or repulsion between atoms (Figure 4).

$(3K - 7)$-dimensional vibrational space:

(5) Dependence of normal mode frequencies on s and identification of avoided mode−mode crossings as well as reaction path bifurcation points (Figure 5).

(6) Adiabatic force constants (and, optional, adiabatic frequencies) associated with the internal parameters chosen to describe the reaction as a function of s (Figure 6).

(7) Decomposition of particular normal modes in terms of adiabatic internal modes along s (Figure 7).

(8) Reaction path curvature $\kappa(s)$ and its decomposition (a) in terms of normal mode curvature coupling coefficients $B_{\mu,s}$ and (b) in terms of adiabatic internal mode curvature coupling amplitudes $A_{n,s}$ (Figure 8a,b).

(9) Analysis of particular mode−mode coupling coefficients $B_{\mu,\nu}$ as a function of s (Figure 9).

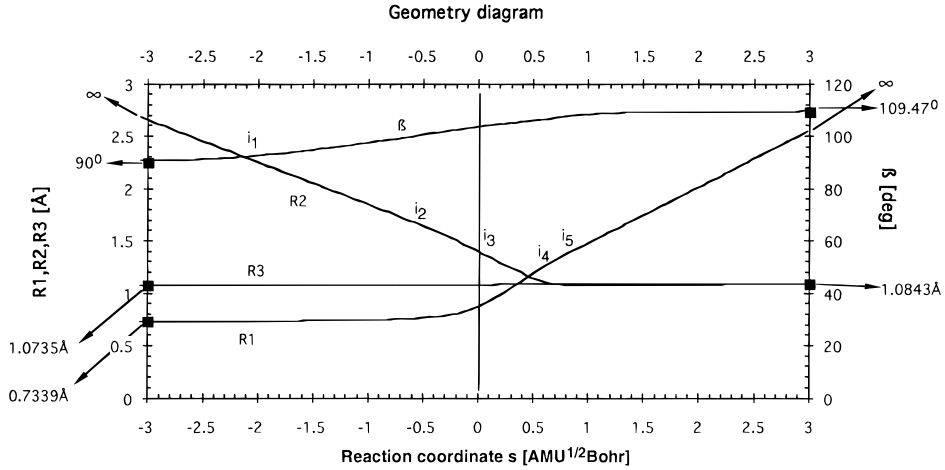

Figure 2. UMP2/6-31G(d,p) geometrical parameters of the reaction complex $CH_3\cdots H_2$ given as a function of the reaction coordinate s. For a definition of parameters, compare with Scheme 2. Geometrical parameters of reactants and products are given on the left and right of the diagram. The position of the transition state corresponds to $s = 0$ amu$^{1/2}$ a_0 and is indicated by a vertical line. Inflection points i_j of the curves R2(s) and R1(s) are indicated (compare with Figure 14).

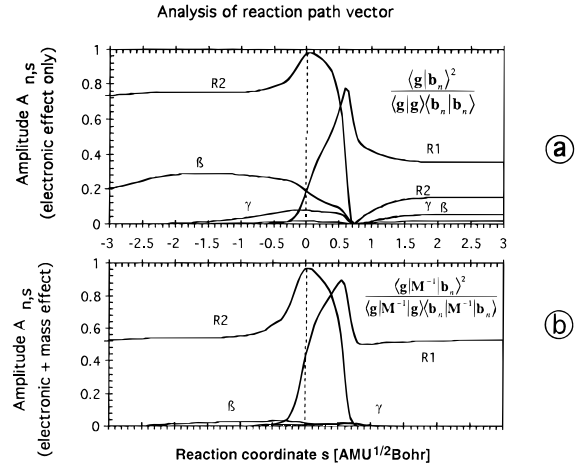

Figure 3. Characterization of the reaction path vector $\boldsymbol{\eta}(s)$ in terms of internal parameter vectors using amplitudes $A_{n,s}$: (a) consideration of electronic effects; (b) consideration of electronic and mass effects. For a definition of parameters, compare with Scheme 2. The position of the transition state corresponds to $s = 0$ amu$^{1/2}$ a_0 and is indicated by a vertical line.

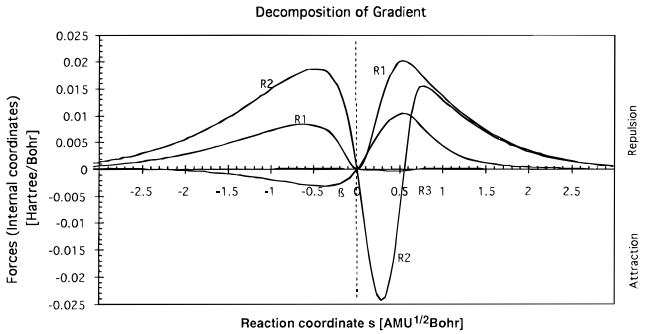

Figure 4. Decomposition of the gradient in terms of attractive or repulsive internal forces. For a definition of parameters, compare with Scheme 2. The position of the transition state corresponds to $s = 0$ amu$^{1/2}$ a_0 and is indicated by a vertical line.

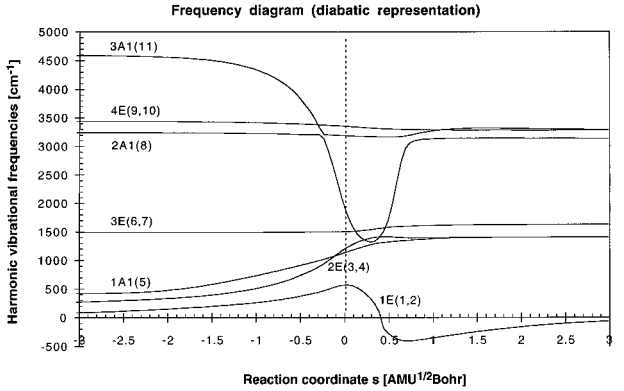

Figure 5. Diabatic representation of normal mode frequencies $\omega_\mu(s)$. Symmetry symbols and numbering of normal modes are given according to the order of normal modes calculated for the reactants. The position of the transition state corresponds to $s = 0$ amu$^{1/2}$ a_0 and is given by a vertical line. The value $\omega_{1e}(s) = 0$ indicates the location of the bifurcation point ($s = 0.4$ amu$^{1/2}$ a_0). Imaginary 1e frequencies calculated for $s > 0.4$ amu$^{1/2}$ a_0 are given as negative numbers.

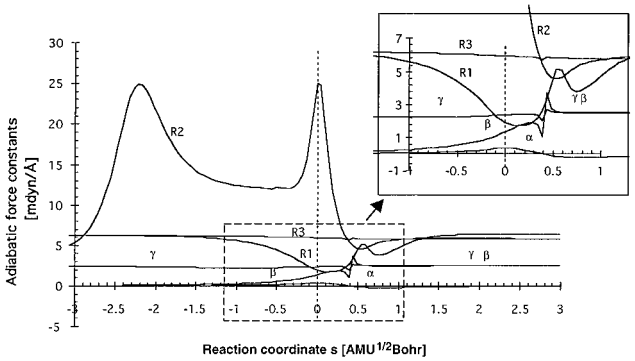

Figure 6. Generalized adiabatic force constants associated with internal parameters described in Scheme 2. The position of the transition state corresponds to $s = 0$ amu$^{1/2}$ a_0 and is indicated by a vertical line. The insert gives the exact position of the bifurcation point at $s = 0.4$ amu$^{1/2}$ a_0.

(10) Mode−mode coupling pattern to describe possible mechanism of energy dissipation between modes (Figure 10).

In each of Figures 1−9, the position of the TS is defined by a dashed vertical line at $s = 0$; i.e., the noninteracting reactants $CH_3 + H_2$ are located at $s = -\infty$ and the noninteracting products $CH_4 + H$ at $s = +\infty$ where because of calculational reasons a much smaller range of s ($s = -3$ to $+3$ amu$^{1/2}$ a_0) is considered. Figures 1−10 are complemented by Figure 11, which shows the electron difference density distribution $\Delta\rho(\mathbf{r},s)$ at selected points of s. The results of the analysis of $\Delta\rho(\mathbf{r},s)$ represent the link between the investigation of the one- and ($3K - 7$)-dimensional part of the harmonic reaction valley and, by this, lead to an unified analysis of the mechanism of reaction I.

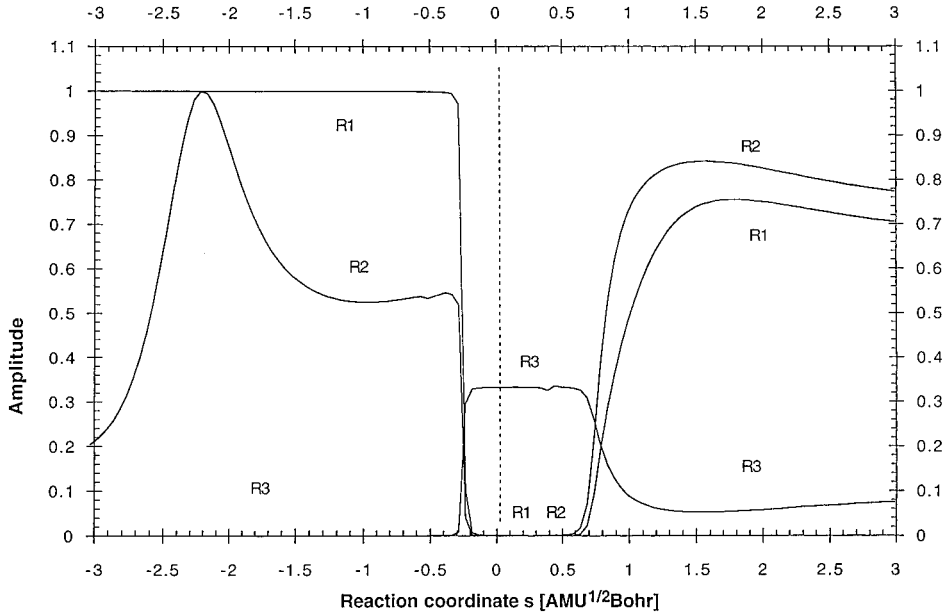

Figure 7. Characterization of the $3a_1$ symmetric mode (mode 11) in terms of generalized adiabatic modes. For a definition of parameters, compare with Scheme 2. The position of the transition state corresponds to $s = 0$ amu$^{1/2}$ a_0 and is indicated by a vertical line.

TABLE 1: Comparison of UMP2/6-31G(d,p) Geometries and Harmonic Frequencies with the Corresponding CCSD(T)/[5s4p3d/4s3p] and Experimental Values[a,b]

		geometry					harmonic frequencies		
molecule	$\zeta_n = q_n$	UMP2	CCSD(T)	exptl	no.	symm	UMP2	CCSD(T)	exptl
H_2, $D_{\infty h}$	R1(HH)	0.734	0.741	0.741	ω_{11}	$1\sigma_g^+$	4609	4409	4405
CH_3, D_{3h}	R3(CH)	1.074	1.076	1.079	$\omega_{9,10}$	$2e'$	3441	3307	3161[c]
					ω_8	$1\alpha_1'$	3243	3125	3002[c]
					$\omega_{6,7}$	$1e'$	1492	1445	1396[c]
					ω_5	$1a_2''$	395	492	606[c]
$H_3C\cdots H_2$, C_{3v}	R2(CH)	1.399	1.393		$\omega_{9,10}$	4e	3355	3229	
	R1(HH)	0.874	0.897		ω_8	$2a_1$	3189	3083	
	R3(CH)	1.080	1.082		ω_{11}	$3a_1$	1925	1763	
	β(HCH)	103.6	103.2		$\omega_{6,7}$	3e	1505	1458	
					$\omega_{3,4}$	2e	1203	1124	
					ω_5	$1a_1$	1137	1093	
					$\omega_{1,2}$	1e	572	518	
					ω_i	a_1	1752i	1500i	
CH_4, T_d	R3(CH)	1.084	1.086	1.086	$\omega_{8,9,10}$	$2t_2$	3282	3153	3158
					ω_{11}	$1a_1$	3135	3037	3137
					$\omega_{6,7}$	1e	1627	1592	1567
					$\omega_{3,4,5}$	$1t_2$	1406	1366	1357

[a] Bond distances in Å, angles in deg, frequencies in cm^{-1}. CCSD(T) and experimental values taken from ref 12. For a definition of geometrical parameters, see Scheme 2. Frequencies are numbered for the reaction complex $CH_3\cdots H_2$ starting at the far left of the $\omega_\mu(s)$ diagram of Figure 5. This numbering is kept for reactants and product. [b] UMP2 energies are −1.15766 (H_2), −40.36986 (CH_4), −39.69753 (CH_3), −40.83252 hartree ($H_3C\cdots HH$). [c] Fundamental (anharmonic) frequencies.

TABLE 2: Analysis of Vibrational, Rotational, and Translational Modes of the Reaction System $CH_3 + H_2 \rightarrow CH_4 + H$

reactants: $CH_3 + H_2$	transition state	products: $CH_4 + H$
1 donating mode: rate enhancement by stimulating HH stretch	mode 11/8 ($3a_1/2a_1$)	accepting mode: rate enhancement of reverse reaction by stimulating CH stretch
6 spectator modes	modes 5−10/5−7, 9−11	6 spectator modes
2 rotations of H_2 (α rotation)	modes 3, 4 (2E)	2 spectator modes
2 rotations of CH_3 (β rotations)	modes 1, 2 (1E)	2 rotations of CH_4 (α rotations)
1 rotation at $CH_3\cdots H_2$ axis	1 rotation at $CH_3\cdots H_2$ axis	1 rotation at $CH_4\cdots H$ axis
2 translations of reactants	2 rotations at axes perpendicular to $CH_3\cdots H_2$ axis	2 translations of products
3 translations of reactants	3 translations of reaction complex	3 translations of products
	Sum of Modes	
7 vibrations	11 vibrations	9 vibrations
1 translation along *s*	1 translation along *s*	1 translation along *s*
5 rotations	3 rotations	3 rotations
5 translations	3 translations	5 translations
18 modes	18 modes	18 modes

In Table 1, UMP2/6-31G(d,p) energies, geometries, and harmonic vibrational frequencies are compared with the available experimental data and data from the CCSD(T) investigation of Kraka and co-workers.[12] Table 2 gives a summary of the generalized CNM analysis, which reveals which normal modes are involved in energy transfer (donator/acceptor modes), which

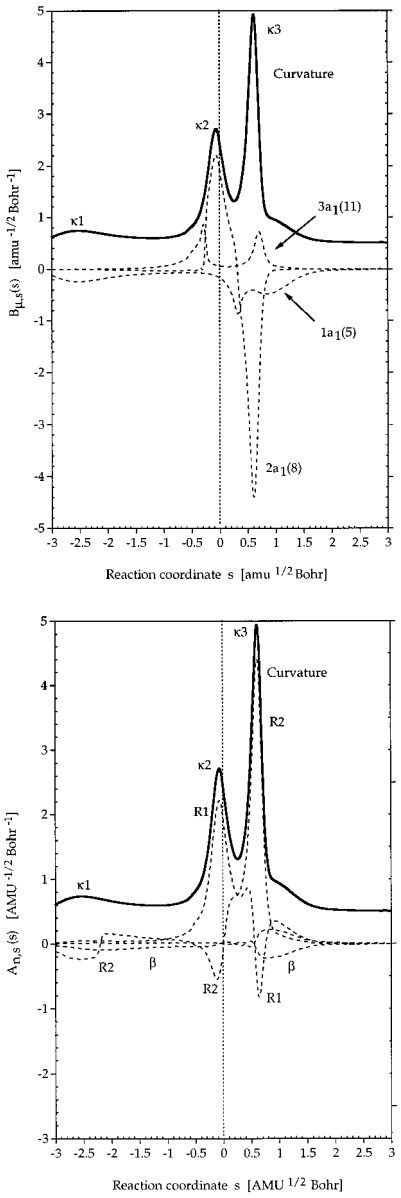

Figure 8. Decomposition of the reaction path curvature $\kappa(s)$ (thick solid line) in terms of (a) normal mode-curvature coupling coefficients $B_{\mu,s}(s)$ (dashed lines) and (b) adiabatic mode-curvature coupling amplitudes $A_{n,s}(s)$ (dashed lines). The curve $\kappa(s)$ has been shifted by 0.5 units to more positive values to facilitate the distinction between $\kappa(s)$, $B_{\mu,s}(s)$, and $A_{n,s}(s)$. For a definition of parameters, compare with Scheme 2. The position of the transition state corresponds to $s = 0$ amu$^{1/2}$ a_0 and is indicated by a vertical line.

modes are not involved in energy transfer (spectator modes), which vibrational modes are converted into rotational modes, etc.

In the following, we will discuss each of the 10 steps of the URVA of reaction I in detail, focusing in particular on the reaction mechanism, possible ways of rate enhancement by curvature coupling, and energy dissipation by mode−mode coupling.

4.1 Analysis of the One-Dimensional Reaction Space. For a chemist, the dependence of energy and geometry on the reaction coordinate s provides the most important information on the reaction mechanism. The diagrams $E(s)$ (Figure 1), $R(s)$, $\beta(s)$, etc. (Figure 2) contain many details as, e.g., steepness (flatness) or curvature of the PES in the direction of a certain q_n coordinate that dominates the reaction path vector $\boldsymbol{\eta}(s)$. It is a common approach to unravel these details by calculating first and second derivatives and carrying out a fine or hyperfine analysis of the functions $E(s)$, $R(s)$, etc.[34] Clearly, the energy

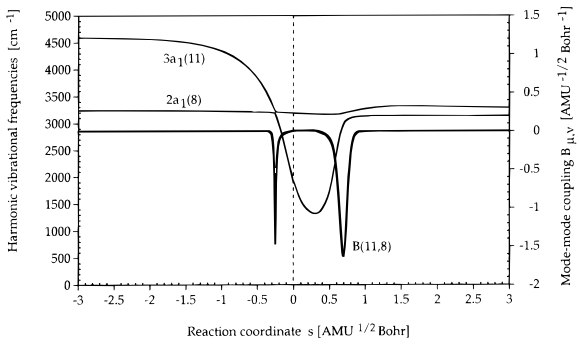

Figure 9. UMP2/6-31G(d,p) frequencies $\omega_\mu(s)$ of the $3a_1$ and $2a_1$ symmetric modes (modes 11 and 8) and the corresponding mode−mode coupling coefficient $B_{11,8}(s)$. The position of the transition state corresponds to $s = 0$ amu$^{1/2}$ a_0 and is indicated by a vertical line.

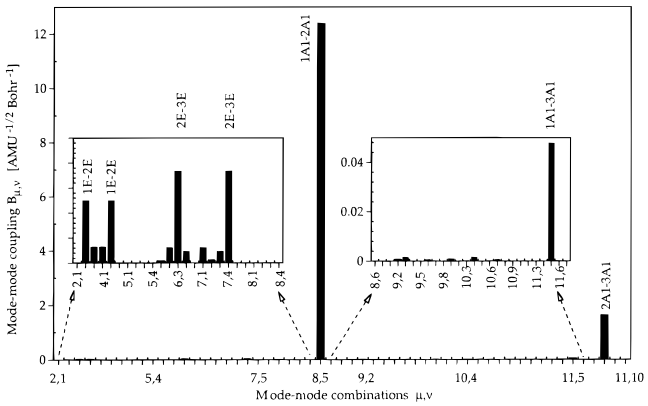

Figure 10. Mode−mode coupling pattern for the reaction system $CH_3 + H_2$. The largest (absolute) value of the coefficient $B_{\mu,\nu}(s)$ is shown for each of the 55 possible mode combinations, which are given on the abcissa in the order 2−1, 3−1, 3−2, 4−1, etc.

profile and the geometry changes along the path $\mathbf{x}(s)$ are central to the following analysis; however, the investigation of the forces or the vectors $\boldsymbol{\eta}(s)$ and $\boldsymbol{\kappa}(s)$ facilitates this task and leads to useful insights into the reaction that can be used to enhance the reaction rate.

Energetics. At UMP2/6-31G(d,p), reaction energy and reaction barrier are calculated to be −8.1 and 14.2 kcal/mol (Figure 1), respectively, which have to be compared with the results of the much more elaborate CCSD(T)/VQZ[3d2f1g/3p2d1f] calculations of Kraka and co-workers[11] who obtained −4.0 and 11.8 kcal/mol.[11] The latter energies still exaggerate exothermicity and barrier of the reaction by 0.9 and 1.8 kcal/mol, respectively, as becomes obvious from calculated and experimental reaction enthalpy at 300 K (−1.5 versus −0.6 kcal/mol) and the corresponding data for the activation enthalpy at 300 K (12.7 versus 10.9 ± 0.5 kcal/mol). Hence, UMP2 exaggerates the exothermicity of the reaction by about 4 kcal/mol and the barrier by 2.4 kcal/mol indicating that the description is reasonable, however, should not be expected to provide more than qualitative or semiquantitative insights. In any case, the UMP2/6-31G(d,p) description is much more reliable than early UHF/STO-3G[15,16,20d] and UHF/4-31G[13] investigations of reaction I and, in addition, compares well with QCISD,[17] DFT,[18] and CASSCF descriptions[19] of I.

Geometry. The equilibrium geometry of CH_3, H_2, and CH_4 are well reproduced at the UMP2/6-31G(d,p) level of theory as can be seen by comparing the data listed in Table 1. At the TS, the distance R2(C1H2) is 1.40 Å while distance R1(HH) is only slightly elongated from 0.73 to 0.87 Å. The local symmetry of CH_3 is reduced from D_{3h} to C_{3v} as a result of pyramidalization and increase of the pyramidalization angles β

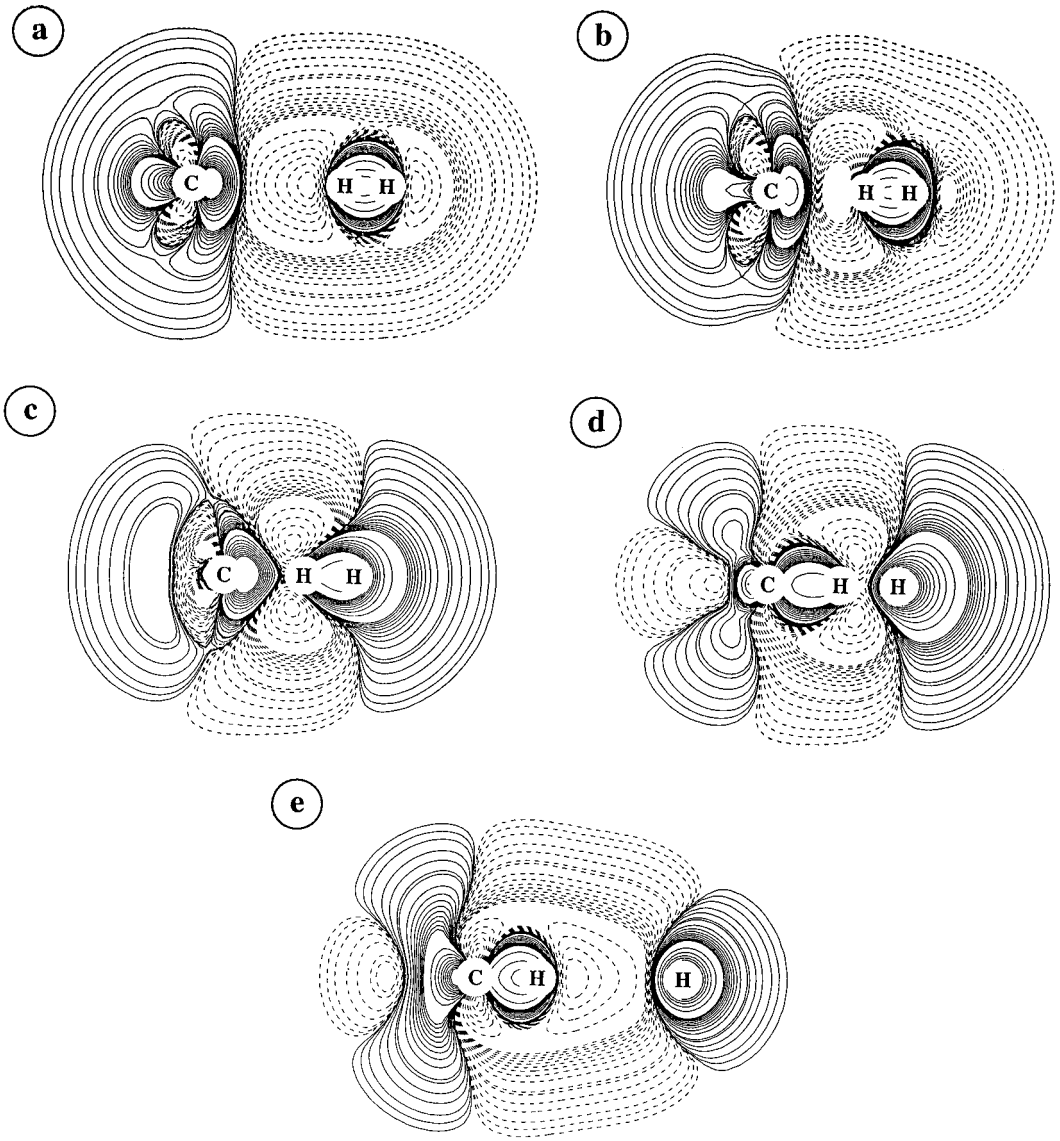

Figure 11. Electron difference density distribution $\Delta\rho(\mathbf{r},s)$ obtained at (a) $s = -3.0$, (b) $s = -0.5$, (c) $s = 0$, (d) $s = 0.3$, and (e) $s = 3.0$ amu$^{1/2}$ a_0. Solid contour lines indicate an increase and dashed contour lines a decrease of electron density relative to the electron density distribution of the procomplex (see text). UMP2/6-31G(d,p) calculations.

(defined in Scheme 2) from 90 to 104°. Figure 2 gives the internal parameters R1(s), R2(s), R3(s), and $\beta(s)$ as functions of the reaction coordinate s. Largest changes are observed for R2(s) (before and slightly after the TS), R1(s) (after the TS), and $\beta(s)$ (before and after the TS), while R3(s) describing changes in the bond lengths CH4, CH5, and CH6 does not varry, which indicates that these bonds are "spectator bonds" that do not participate in the reaction.

Of particular interest are those regions of s in which the "actor bond" R1 (R2) starts to leave (to adopt) its previous (new) equilibrium value. In these regions, the largest curvature of the functions R1(s) ($-0.2 \le s \le 0.3$ amu$^{1/2}$ a_0) and R2(s) ($0.5 \le s \le 0.7$ amu$^{1/2}$ a_0) is encountered, which indicates that the corresponding bond is beginning to break (R1) or finishing its formation (R2). This can be more clearly seen in the curvature diagram of Figure 8. There are also a number of fine variations in R1(s) and R2(s) (changes in gradient and curvature), which are difficult to discuss on the basis of Figure 2 but nevertheless indicate important electronic structure changes. They can be made visible when analyzing $\boldsymbol{\eta}(s)$ and $\kappa(s)$.

Reaction Path Vector. When electronic effects on the direction of $\boldsymbol{\eta}(s)$ are considered according to eq 31 (Figure 3a), parameters R1 and R2 represent the most important contributions to the reaction path vector, while the bond angle parameters β and γ lead to much smaller but significant contributions. This is reasonable insofar as breaking of the HH bond (described by R1) and formation of the CH bond (described by R2) are accompanied by small changes in the angles and an overall change in the electronic structure of the reaction complex. When mass effects are included in the analysis of $\boldsymbol{\eta}(s)$ (kinetic analysis according to eq 30), contributions from angle parameters become vanishing small (Figure 3b), leaving as important reaction parameters only R1 and R2 which asymptotically describe the separation of H from CH_4 ($s \rightarrow +\infty$) and H_2 from CH_3 ($s \rightarrow -\infty$). The ratio of contributions from R1 and R2 and the appearance of maximal contributions from either R1 or R2 close to the TS are interesting features of Figure 3a,b, which we will discuss in connection with the analysis of the reaction path curvature $\kappa(s)$.

Internal Forces. At the three stationary points along the reaction path, all internal forces have to be zero, which according to Figure 4 is fulfilled for the reactants ($s \rightarrow -\infty$) and products in their equilibrium geometries ($s \rightarrow +\infty$) as well as the TS ($s = 0$). In all other regions along the reaction path, the internal forces adopt either positive values indicating atom−atom repulsion or negative values indicating atom−atom attraction.

Again, the largest forces are associated with R1 and R2, smaller forces with β, and negligible forces with R3, thus confirming the differentiation between actor and spectator bonds.

Figure 4 reveals that interaction forces between H2 and H3 (parameter R1) before and after the TS are always repulsive with maximal values at $s = \pm 0.5$. On the other hand, interactions between atoms C1 and H2 (parameter R2) are both repulsive (maxima at $s = -0.5$ and $s = 0.8$ amu$^{1/2}$ a_0) and attractive (minimum at $s = 0.3$ amu$^{1/2}$ a_0). The changes of the interacting forces along the reaction path shown in Figure 4 can be explained with the help of the difference density distributions $\Delta\rho(\mathbf{r},s)$ at selected values of s shown in Figure 11.

When the reacting molecules approach each other (Figure 11a, $s = -3$ amu$^{1/2}$ a_0), the dominant interaction is exchange (overlap) repulsion that leads to a depletion of electron density in the region between the molecules as indicated by a negative $\Delta\rho(\mathbf{r})$ distribution (dashed lines in Figure 11a). Exchange repulsion increases with decreasing distance between CH_3 and H_2, and as a consequence, electron density is pushed from the front side of H2 to the back of H3; i.e. the HH bond starts to become polarized (Figure 11b, $s = -0.5$ amu$^{1/2}$ a_0). This is the point at which induction forces caused by the buildup of negative charge at C1 and the induced $H2^{\delta+}-H3^{\delta-}$ dipole moment begin to compensate part of the exchange repulsion. Figure 11c gives the situation of the TS, at which attractive induction forces and repulsive exchange forces exactly compensate each other. At this point, polarization of the HH bond has proceeded to a point that a significant amount of electron density begins to flow out of the bond region; i.e. the breaking of the HH bond has started (compare with Figure 2 and the upward curving of R1(s)). At the same time, the negative charge at C is polarized into the direction of H2, which represents the positive end of the HH bond dipole.

At $s = 0.3$ amu$^{1/2}$ a_0 (Figure 11d), the positive difference electron density fills the space between C1 and H2 while a region of negative difference electron density appears between H2 and H3. At this point, the H−H bond dipole moment adopts its largest value and inductive attraction between C1 and H2 is at its maximum (according to a minimum of the R2 force, Figure 4). For larger values of s, electron density at H2 increases again, the value of the HH dipole moment and with it inductive attraction decrease, and at the same time exchange repulsion between H2 and C1 increase toward a maximum at $s = 0.8$ amu$^{1/2}$ a_0. In this region the formation of the new C1H2 bond is finished, and charge distribution between C1 and H2 rapidly approaches the normal situation of a CH bond in CH_4 (Figure 4e).

The changes in the R1 force curve can similarly be investigated with the help of the $\Delta\rho(\mathbf{r})$ distribution considering the reverse reaction. The induction forces between H atom and CH_4 are considerably smaller than those between H_2 and CH_3, and therefore, just a balance between attractive and repulsive forces is reached at the TS without leading to a dominance of attractive force contributions (negative force values) for R1.

The $\Delta\rho(\mathbf{r})$ distributions of Figure 11 also explain why the internal force associated with pyramidalization angles β are slightly negative for $s < 0$ before they reach a repulsion maximum at $s = 0.5$. Upon approach of H_2, the planar CH_3 radical starts to pyramidalize and pyramidalization increases β, thus avoiding most of the exchange repulsion between H_2 molecule and the H atoms of the CH_3 radical. Beyond the TS the increase of the pyramidalization angle becomes slower while exchange repulsion with decreasing C1,H2 distance rapidly increases, thus causing a maximum in the force curve for β.

4.2 Analysis of the Reaction Valley. The investigation of the $(3K - 7)$-dimensional vibrational space is not only important in connection with the description of energy transfer and energy dissipation but also for the understanding of features of the PES along the reaction path as well as changes in the geometry of the reaction complex. This becomes in particular clear when comparing Figures 2 (geometry) and 3 (characterization of $\boldsymbol{\eta}(s)$) with Figure 8 (characterization of $\kappa(s)$) or Figures 1 (energy profile) and 4 (forces) with Figure 6 (adiabatic force constants).

Normal Mode Frequencies. Trends in the normal mode frequencies have been investigated by several authors before[13,16−18,20b,c,g,l,n] and, therefore, should only briefly considered here. The ordering of normal modes is done utilizing the symmetry of the C_{3v}-symmetrical reaction complex and numbering modes from large to small according to the order they have in the entrance channel of the reaction (Figure 5, Table 1). As mentioned in section 3, the diabatic mode ordering (DMO) method[28] used for the generation of the curves $\omega_\mu(s)$ shown in Figure 5 automatically resolves all avoided crossings between modes of identical symmetry by reducing the step size in the vicinity of the avoided crossing point. For example, at $s = -0.3$ amu$^{1/2}$ a_0 there is an avoided crossing between the $3a_1$- and $2a_1$-symmetrical mode (modes 11 and 8, Figure 5). Since mode−mode interactions are strongly localized at this point (weak interactions), the curves ω_μ(s) approach each other rather closely before they depart again. As a consequence, the step size has to be reduced to 0.01 amu$^{1/2}$ a_0 to get a correct description of this region. The avoided crossings at $s = 0.35$ (modes 5 and 8) and 0.7 amu$^{1/2}$ a_0 (modes 8 and 11) involving a_1-symmetrical modes are less problematic in this respect since mode−mode interactions are more delocalized (stronger) and the avoided crossings are resolved at a larger step size.

Clearly, the combination ω_{11}/ω_8 (ω_{11} before, ω_8 after the avoided crossing) possesses the largest changes in the TS region (Figure 5), and therefore, it must be related to the HH and CH stretching modes associated with coordinates R1 and R2. This has been observed and discussed by other authors.[13−20] Also, it has been pointed out that $\omega_\mu(s)$ for the degenerate 2e modes (no. 3 and 4) becomes imaginary for $s > 0.4$ amu$^{1/2}$ a_0 (indicated in Figure 5 by negative ω_μ(s) values) because of a bifurcation point at $s = 0.4$ amu$^{1/2}$ a_0. This bifurcation point is actually a trifurcation point since the reaction valley splits at this point into three separated reaction valleys accompanied by a reduction of the symmetry of the reaction complex from C_{3v} to C_s (atom H3 moves first toward the bisector of angle H2C1H4, H2C1H5, or H2C1H6 and later to one of the three faces of methane on the C1H2 side because exchange repulsion is smaller in these directions). Since the path chosen in this work conserves C_{3v} symmetry, it follows the energy ridge separating the reaction valleys. However, the energy differences between ridge path and valley paths are so small that the description obtained for the ridge path is largely valid for the valley paths.

Adiabatic Force Constants. Since force constants directly reflect properties of the electronic structure of a molecule while the corresponding frequencies also cover mass effects, we concentrate in the following just on the former. By construction, the generalized adiabatic force constants $k_n^a(s) = k_a[q_n](s)$ associated with internal parameters $\zeta_n = q_n$ that are used to describe the reaction complex cover two different effects:

(a) First, they describe the curvature of the reaction valley, i.e. the curvature of the PES in the $3K - 7$ directions transverse to the reaction path;

(b) Second, they are influenced by the projection of the vibrational modes from $(3K - L)$-dimensional space to $((3K - L)$-1)-dimensional space.

The projector $\mathbf{I}-\mathbf{P}(s)$ projects onto the $((3K - L) - 1)$-dimensional space spanned by the normal modes, which are

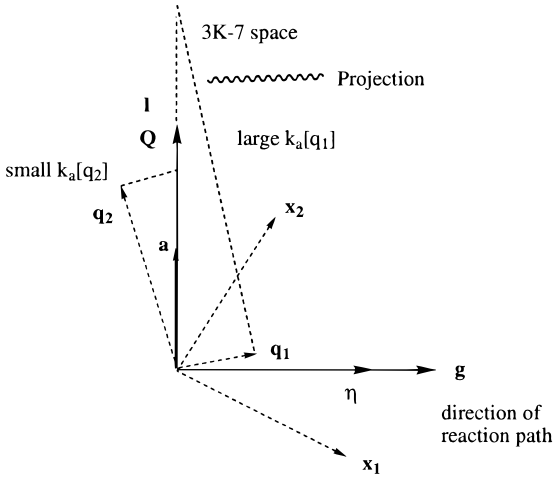

Figure 12. Schematic representation of reaction path space and the orthogonal space of the transverse normal modes for a hypothetical two-dimensional problem. Cartesian coordinates are denoted by x_1 and x_2, internal coordinates by q_1 and q_2, gradient by **g**, reaction path vector by $\boldsymbol{\eta}$, the normal mode vectors by **l**, and the adiabatic mode vector by **a**. The projection needed to obtain adiabatic force constants $k_a[q_1]$ and $k_a[q_2]$ is indicated by dotted lines.

orthogonal to the reaction path vector. One can consider the $((3K - L) - 1)$-dimensional vibrational space as a (hyper)-plane, the normal vector of which is the reaction path vector. The internal coordinates associated with the internal vibrational modes are not located in this plane (Figure 12). If the direction of an internal vibrational mode vector (in $(3K - L)$-space) associated with an internal coordinate is more or less orthogonal to the direction of the vector $\boldsymbol{\eta}(s)$ (q_2 in Figure 12), then its projection onto the $((3K - L) - 1)$-dimensional subspace will not change the corresponding generalized adiabatic force constant k_a^g significantly, and therefore, the value of k_a^g will be similar to that calculated for an equilibrium geometry.

However, if the direction of an internal mode vector largely coincides with the direction of the reaction path vector $\boldsymbol{\eta}(s)$ (q_1 in Figure 12), then projection onto the $(3K - 7)$-dimensional subspace will lead to a large generalized adiabatic force constant k_a^g, which clearly exceeds the values found for equilibrium geometries. In this way, contributions from a and b determine the actual value of the generalized adiabatic force constants (see Figure 12).

In particular with regard to the latter situation, the generalized adiabatic force constants are sensitive tools that reveal changes of the PES and in particular of the reaction path valley that are directly related to changes in the electronic structure of the reaction complex and, therefore, are of chemical relevance.

Figure 6 presents the calculated generalized adiabatic force constants for reaction I. Apart from the values of the generalized adiabatic force constant associated with distance R2 in the entrance channel of the reaction (k_a[R2] > 10 mdyn/Å), all other force constant values are <7 mdyn/Å and, therefore, resemble those of equilibrium geometries. Hence, k_a[R2] is the force constant that provides insight into the features of the PES and the direction of the reaction valley. Close to the TS, k_a[R2] possesses a maximum of about 26 mdyn/Å before it drops to a value typical of a CH bond in CH_4. The maximum at $s = 0$ amu$^{1/2}$ a_0 indicates that (in the forward direction) the R2 mode, which up to this point is basically a translational mode (see Figure 3), becomes a vibrational mode associated with a strong reorganization of electronic structure and the establishment of a CH bond. This is parallel to a R2 maximum in the decomposition of the reaction path vector $\boldsymbol{\eta}(s)$ (Figure 3). The width of the adiabatic force constant peak at the TS indicates how fast the reaction system adjusts to this change.

While the peak of k_a[R2] at the TS is what one expects, the occurrence of a second, equally high, but much broader peak at $s = -2.2$ amu$^{1/2}$ a_0 (beginning at $s = -2.9$ and ending at $s = -1.5$) is rather unexpected considering that in this region there is no local minimum of the PES (Figure 1). However, the k_a[R2] peak in the entrance channel indicates the "preparation" of the reacting molecules for the reaction. For $s < -2.5$ amu$^{1/2}$ a_0, one cannot speak of a reaction or a reaction coordinate since the approach parameter is arbitrarily fixed by assuming a certain symmetry and configuration for the reacting system. Vibrational motions are localized within the subunits of the reaction system and any relative motion is constrained to be just translational or rotational. At the first k_a[R2] peak, the local symmetry, the geometry, and the electronic structure of one (or both) reactant(s) change. The reaction coordinate becomes dominated by the R2 internal coordinate that keeps this role up to the TS (Figure 3), where it changes to become the internal parameter of a new vibrational mode.

In the region of the first k_a[R2] peak, the geometry of CH_3 changes from a planar (local D_{3h} symmetry) to a pyramidal form (local C_{3v} symmetry) under the impact of the approaching H_2 molecule. This is accompanied by a major electronic change involving the transformation of a pure π-radical to a σ-radical as is indicated by the relatively large height of the R2 force constant maximum (Figure 6). The reaction path vector is dominated by R2 and an increasing β component (Figure 3) where β is the pyramidalization angle (Scheme 2).

The width of the R2 peak at $s = -2.2$ amu$^{1/2}$ a_0 indicates that pyramidalization contrary to bond cleavage is a slow process. This can easily be understood considering the fact that at a distance of 2−2.5 Å (Figure 2) between the reacting molecules interactions are moderate and only slowly increase with decreasing value R2.

Another important feature of Figure 6 is the functional dependence of the generalized adiabatic force constant associated with the two bending angles α (Scheme 1). The value of $k_a[\alpha]$ becomes negative at $s = 0.4$ amu$^{1/2}$ a_0, which is the location of the bifurcation point. Both constants $k_a[\beta]$ and $k_a[\gamma]$ are sensitive to reaction path bifurcation as can be seen by the wiggle in the $k_a(s)$ curves (inset in Figure 6). For $s > 0.4$ amu$^{1/2}$ a_0, the path follows the energy ridge between three reaction valleys, for which the partitioning of the space into one-dimensional and $(3K - 7)$-dimensional orthogonal subspace is still useful. Since the PES is relatively flat in the direction of internal parameter α, it does not pay off to start a new IRC path at the bifurcation point to follow one of the new valleys. All generalized adiabatic modes but that for α and R1 remain basically unchanged by walking either along the ridge or one of the valleys. For k_a[R1], there is a small peak at $s = 0.6$ amu$^{1/2}$ a_0, which would probably become larger if walking along a valley; however, this is of no practical relevance. It corresponds to a delayed reorganization of the electronic structure of CH_4 under the impact of the approaching H atom that is too weak to develop at a typical H,H van der Waals distance of 2.4 Å.

Decomposition of Normal Modes in Terms of Adiabatic Internal Modes. To describe normal modes in terms of adiabatic internal modes, the amplitude $A_{n,s}(s)$ is defined[9,10]

$$A_{n,s}(s) = \frac{(\mathbf{I}_\mu(s)^+ \mathbf{F}(s)\, \mathbf{a}_n(s))^2}{(\mathbf{I}_\mu(s)^+ \mathbf{F}(s)\, \mathbf{I}_\mu(s))(\mathbf{a}_n(s)^+ \mathbf{F}(s)\, \mathbf{a}_n(s))} \qquad (35)$$

In Figure 7, as an example the $3a_1$ mode (mode 11) is analyzed. For $s < -0.2$ amu$^{1/2}$ a_0, the $3a_1$ mode is a typical HH stretching

mode that becomes for $s > 0.7$ amu$^{1/2}$ a_0 a CH stretching mode. At $s = -2.2$ amu$^{1/2}$ a_0, there is a large contribution of the R2 internal stretching mode identifying that point of the reaction path where the CH_3 radical changes its geometry and electronic structure and, thereby, "couples" via the R2 motion to the approaching H_2 molecule. Hence, the maximum of the adiabatic force constant associated with R2 results from mode 11 and the coupling of the HH and CH stretching modes.

The two avoided crossings at $s = -0.3$ and $s = 0.7$ amu$^{1/2}$ a_0 are responsible for the sudden changes in the decomposition of mode 11 at these points (Figure 7) and explain why mode 11 first corresponds to the HH stretching mode (internal coordinate R1), then to the CH stretching mode of a spectator bond (R3, previously mode 8), and, finally, to the streching mode of the newly formed CH bond (R2). Complementary changes can be found in the decomposition of mode 8. For example, at $s = 0.4$ the HH stretching contribution to mode 8 becomes very small and the R2 stretching motion increases to a maximum at $s = 0.55$. This is exactly the region where the HH bond is broken and the CH bond formed. The decomposition of a delocalized normal mode in terms of localized adiabatic modes unravels how the character of the normal mode changes during the course of the reaction. In this way, the correlation between reactant and product modes becomes straightforward.

Reaction Path Curvature. The reaction path curvature $\kappa(s)$ is shown in Figure 8a as a function of s. As found by other authors,[13−20] there are two distinct peaks of $\kappa(s)$ in the TS region at $s = -0.1$ and 0.7 amu$^{1/2}$ a_0 (peaks $\kappa 2$ and $\kappa 3$), which are associated with mode 11/8 (i.e. 11 before and 8 after the avoided crossing at $s = -0.3$) and to some smaller extend with modes 5 and 8/11 as the decomposition of $\kappa(s)$ in terms of normal mode contributions reveals. If energy is stored in mode 11/8, it will be channeled into the reaction path mode and lead to rate acceleration. Dissipation of energy into mode 8/11 is small since the avoided crossing between modes 11 and 8 at s $= -0.3$ amu$^{1/2}$ a_0 is strongly localized and, therefore, the exchange of energy rather limited.

In the case of reaction I, it is easy to determine the nature of modes 11 and 8 and, in this way, to relate the peaks of the curvature vector with the corresponding changes in electronic structure. However, in general this way of analysis is difficult, and therefore, we introduce a new way of analyzing $\kappa(s)$ that is based on a decomposition of the curvature vector in terms of generalized adiabatic internal modes described in section 2 (Figure 8b). Using this decomposition of $\kappa(s)$, properties of the reaction path curvature, in particular those not found in previous work,[13−20] will be discussed in detail.

There is a small curvature maximum at $s = -2.5$ (peak $\kappa 1$, Figure 8), which starts to develop at -2.9 and drops out at -1.5, i.e. exactly in that range where the maximum of the generalized adiabatic force constant associated with R2 is found. The maximum in the curvature is dominated by a negative adiabatic R2 component, which means that curvature vector and adiabatic mode vector are collinear but point in opposite directions indicating that the reaction system resists a shortening of the R2 distance since this implies pyramidalization of CH_3. Once the pyramidalization of CH_3 is initiated and attractive induction forces start to develop (see Figure 11 and discussion of forces), the R2 adiabatic mode vector rotates into the direction of the curvature vector $\kappa(s)$ (at $s > -2.2$ amu$^{1/2}$ a_0).

Within a relatively short range ($-2.5 < s < -2.1$ amu$^{1/2}$ a_0), the first step of CH_3 pyramidalization is accomplished accompanied by an accelerated decrease of R2 (Figure 14). However, further decrease of R2 requires stronger pyramidalization and a polarization of H_2 which is resisted by the reaction complex. In the range $-2.5 < s < -0.2$, the curvature coefficient A[R2] decreases from small positive to small negative values (Figure 8b). In this region, $\boldsymbol{\eta}(s)$ is dominated by R2 while the magnitude of k_a[R2] (Figure 6) remains relatively large, thus indicating that a translational mode is going to be converted into a vibrational mode. This conversion starts close to the TS where another maximum in k_a[R2] is encountered and the R2 component of the reaction path vector starts to increase to a maximum: The CH bond begins to be formed, and at the same time a R1 peak of $\kappa(s)$ (peak $\kappa 2$) is encountered at $s = -0.05$ amu$^{1/2}$ a_0, which means that the HH bond starts to break (Figure 8b). It is important to note that HH bond breaking and CH bond forming are not independent of each other as is clearly revealed by the characterization of $\kappa(s)$ in terms of adiabatic components: The positive R1 contribution to $\kappa 2$ is accompanied by a negative but much smaller R2 contribution, which can be interpreted as indication that the reaction system resists a further decrease in R2 needed for the formation of the CH bond. Actually, this resistance precedes the peak $\kappa 2$. Once the HH bond starts to break, A[R2] becomes also larger.

From the second to the third curvature maximum at $s = 0.6$ amu$^{1/2}$ a_0 (peak $\kappa 3$), the R2 and R1 amplitudes $A_{n,s}$ exchange their role; i.e., the R2 amplitude becomes dominant and positive while the R1 amplitude is relatively small and negative. Peak $\kappa 3$ identifies the point where the CH bond-forming process is basically finished if the reaction $CH_3 + H_2$ is considered; for the reverse reaction $CH_4 + H$, it is the point where the C1H2 bond starts to be broken accompanied by the resistance of the electronic structure to form as a new bond the HH bond associated with R1. This interpretation is supported by the fact that at $s = 0.6$ amu$^{1/2}$ a_0 the R2 amplitude of $\boldsymbol{\eta}(s)$ drops from a large value to a zero value (Figure 3).

If one considers the changes in $\kappa(s)$ (Figure 8b) parallel to those in $\boldsymbol{\eta}(s)$ (Figure 4) and $k_a(s)$ (Figure 6), a clear picture of the HH bond-breaking and CH bond-forming process emerges: These processes occur in the region of the curvature peaks $\kappa 2$ and $\kappa 3$ ($-0.1 < s < 0.6$) as indicated by maxima or minima of the amplitudes associated with the internal parameters R1 and R2 describing these bonds, by the maxima of the R2 and R1 amplitudes of the reaction path vector, and the TS maximum of force constant k_a[R2] (and a smaller one of k_a[R1]).

Mode−Mode Coupling. In Figure 9, the coupling coefficient $B_{\mu,\nu}$ for the a_1-symmetrical modes 11 and 8 is plotted as a function of the reaction coordinate s. There are distinct couplings at the positions of the two avoided crossings. In line with the discussion in connection with the curves $\omega_\mu(s)$ (Figure 5), interactions between the two a_1 modes are relatively weak and localized (narrow peak) at $s = -0.3$ amu$^{1/2}$ a_0 (Figure 9) while they are stronger and more delocalized (broad peak) at $s = 0.7$ amu$^{1/2}$ a_0 (Figure 9).

Significant mode−mode coupling leads to energy dissipation from one vibrational mode to the other where dissipation is more effective when the modes interact for a larger range of s values (the interaction is more delocalized). This will be of importance if one tries to enhance the reaction rate by channeling energy into vibrational mode 11/8 (e.g. by tuning a laser onto the frequency ω_{11} of the reactants; Table 1) that couples with the reaction mode as revealed by the reaction path curvature $\kappa(s)$ (Figure 8a). Part of this energy will be dissipated into vibrational mode 8/11 (Figure 5) because of the 8,11-coupling at $s = -0.3$ amu$^{1/2}$ a_0. However, since the coupling is strongly localized, energy dissipation will be small so that rate enhancement is still effective. This is different for the reverse reaction. Energy stored in mode 11/8 (the CH stretching mode) is largely dissipated because of the strong (delocalized) mode−mode

coupling at 0.3 (modes 5 and 8) and, also, the one at 0.7 amu$^{1/2}$ a_0 (modes 8 and 11) where the latter has a smaller effect in view of a relatively small $B_{8,11} = 1.5$ amu$^{-1/2}$ a_0^{-1} (Figure 9). Using the adiabatic mode decomposition, it can easily be checked what changes of the reaction complex have to be done to prevent unwanted energy dissipation. For example, substitution by deuterium reduces energy dissipation considerably, and therefore, energy channeled into mode 11 strongly enhances the reaction rate.

Mode−Mode Coupling Pattern. While diagrams of $B_{\mu,\nu}(s)$ like the one shown in Figure 9 provide detailed insight into possible mode−mode couplings along the reaction path, a generation of all possible $B_{\mu,\nu}(s)$ diagrams for larger reaction systems becomes prohibitive. Therefore, Figure 10 is used to give an overview over the total mode−mode coupling pattern. In Figure 10, the largest (absolute) value of $B_{\mu,\nu}(s)$ is shown for each combination of normal modes $\mathbf{l}_\mu$ and $\mathbf{l}_\nu$ given on the abcissa in the order 2−1, 3−1, 3−2, 4−1, etc. For reaction I, there are just two couplings that are of interest, namely the coupling between the $1a_1$- and $2a_1$-symmetrical modes (modes 5 and 8, $B_{5,8} = 12.2$ amu$^{-1/2}$ a_0^{-1}) at $s = 0.3$ amu$^{1/2}$ a_0 and the one at $s = 0.7$ amu$^{1/2}$ a_0 between modes 8 ($2a_1$) and 11 ($3a_1$) (Figure 9). Clearly, the strongest energy dissipation will involve modes 5 and 8, which is of relevance for the reverse reaction. All other mode−mode couplings (shown in the insert of Figure 10) are smaller than 0.05 amu$^{-1/2}$ a_0^{-1} and, therefore, play a minor role in energy dissipation.

5. Discussion of the Reaction Mechanism

Although the TS is energetically the most important point of the reaction, mechanistically it is not since it represents just one point in the range of the curvature peaks (Figure 8) associated with HH bond breaking and CH bond forming. Mechanistically, it is better to speak of a *transition state region* rather than a TS point since the whole region between the curvature peaks is mechanistically relevant. Using the diagram of $\kappa(s)$ shown in Figure 8, one can distinguish between five different regions, which correspond to different phases of the reaction and different types of the electronic structure of the reaction complex:

(1) *Reactant region* (to the left of curvature peak $\kappa 1$ at $s = -2.5$ amu$^{1/2}$ a_0; R2 > 2.5 Å): very weak interactions between reactants without any chemical relevance; the reactants possess electronic structures that basically correspond to those of the equilibrium geometries.

(2) *Van der Waals region on reactant side* ("preparation region" between curvature peaks $\kappa 1$ and $\kappa 2$; see Figure 8): the reactants prepare for the reaction under the impact of increasing interactions; pyramidalization of CH_3 and polarization of H_2 occurs.

(3) *Transition state region* (between curvature peaks $\kappa 2$ and $\kappa 3$; see Figure 8): bonds are broken or formed.

(4) *Van der Waals region on the product side* ("finalization region" for the forward or "preparation" region for the reverse reaction): the products prepare for the reverse reaction under the impact of increasing interactions. This region is poorly developed for reaction I.

(5) *Product region* (to the right of curvature peak $\kappa 3$ for $s >$ 2 amu$^{1/2}$ a_0; R1 > 2 Å): very weak interactions between products without any chemical relevance.

In general, it will be easy to identify the TS region even if this is strongly displaced from the actual TS. The TS region is characterized by bond-breaking and bond-forming processes and, therefore, characterized by large curvature peaks where one can imply that the magnitude of a curvature peak is related to the magnitude of the electronic structure change represented by a given internal coordinate.

The TS region is not centered at the location of the TS but displaced according to the energetics of reaction I (Figure 1). The displacement of the TS region can be discussed considering the Hammond postulate, which suggests that for an exothermic reaction the TS has properties closer to those of the reactants rather than those of the products ("early TS"). This implies that at the TS the strong electronic changes that take place during a reaction are just initiated as confirmed by the curvature vector $\boldsymbol{\kappa}(s)$ and the reaction path vector $\boldsymbol{\eta}(s)$. The midpoint of the TS region is located at $s = 0.3$ amu$^{1/2}$ a_0 indicated by the crossing of the R1 and R2 amplitude of $\kappa(s)$ (Figure 8b). This means that the position of the TS is shifted by $\Delta s = -0.3$ amu$^{1/2}$ a_0 relative to the center of the TS region into the entrance channel. Hence, the early character of the TS can quantitatively be specified utilizing the characterization of curvature and reaction path vector in terms of internal modes as done by URVA.

Also relevant in connection with the Hammond postulate is the height of curvature peaks $\kappa 2$ and $\kappa 3$ in the TS region. One could speculate that the height reflects the strength of the HH bond being broken and the CH bond being formed. However, this is only indirectly true as becomes obvious from a number of investigations carried out with URVA.[35] The height of the curvature peaks simply indicates the resistance of the reaction system to carry out the electronic structure changes associated with bond breaking or bond forming. Obviously, HH bond breakage in the forward reaction is much easier than CH bond breakage in the reverse reaction, which is directly related to the fact that mutual polarization of H_2 and CH_3 is much easier (peak $\kappa 1$ at $s = -2.5$ amu$^{1/2}$ a_0) than mutual polarization of CH_4 and H (no extra curvature peak in the exit channel).

The fact that the height of the R2 curvature peak is almost twice as large as that of the R1 curvature peak in the TS region directly reveals the stiffness of the reaction complex with regard to the necessary electronic structure changes and, accordingly, is related to energy barriers (Figure 1) of 14 kcal/mol in the forward reaction but 22 kcal/mol in the reverse reaction. In other words, the ratio of the heights of the curvature peaks $\kappa 2$ and $\kappa 3$ together with the position of the TS in the TS region directly reveals the exothermic nature of the reaction and the nature of the TS as an early TS shifted by 0.3 amu$^{1/2}$ a_0 into the entrance channel.

The *van der Waals region on the product side* (finalization region) seems to be missing as a consequence of the considerable stiffness of the reaction complex to electronic structure changes in the reverse reaction. Preparation of the CH_4 molecule for the reaction with H implies its distortion from local T_d symmetry to local C_{3v} symmetry due to interactions with the incoming H atom. Such a process actually exists although it occurs rather close to the R2 curvature peak in the region between $s = 1.5$ and 0.8 amu$^{1/2}$ a_0. In this region, a shoulder of the R2 curvature peak exists, which is associated with the R1 and β adiabatic modes (Figure 8b). The HCH angle β starts to decrease from 109° to some smaller value, which means that locally CH_4 adopts C_{3v} symmetry. Decomposition of the reaction path vector reveals that R1 starts to gain importance at $s = 1.5$ until it increases very rapidly at $s = 0.7$ amu$^{1/2}$ a_0.

The analysis of $\kappa(s)$ in terms of generalized adiabatic modes indicates that there is indeed a *van der Waals region on the product side* although it is not very pronounced and limited to a rather small region of s. This is in line with the fact that CH_4 is much more difficult to distort by a H atom than CH_3 by H_2. For the reaction $CH_4 + H$, the incoming reaction partner H has to come as close as possible which leads right away to CH bond

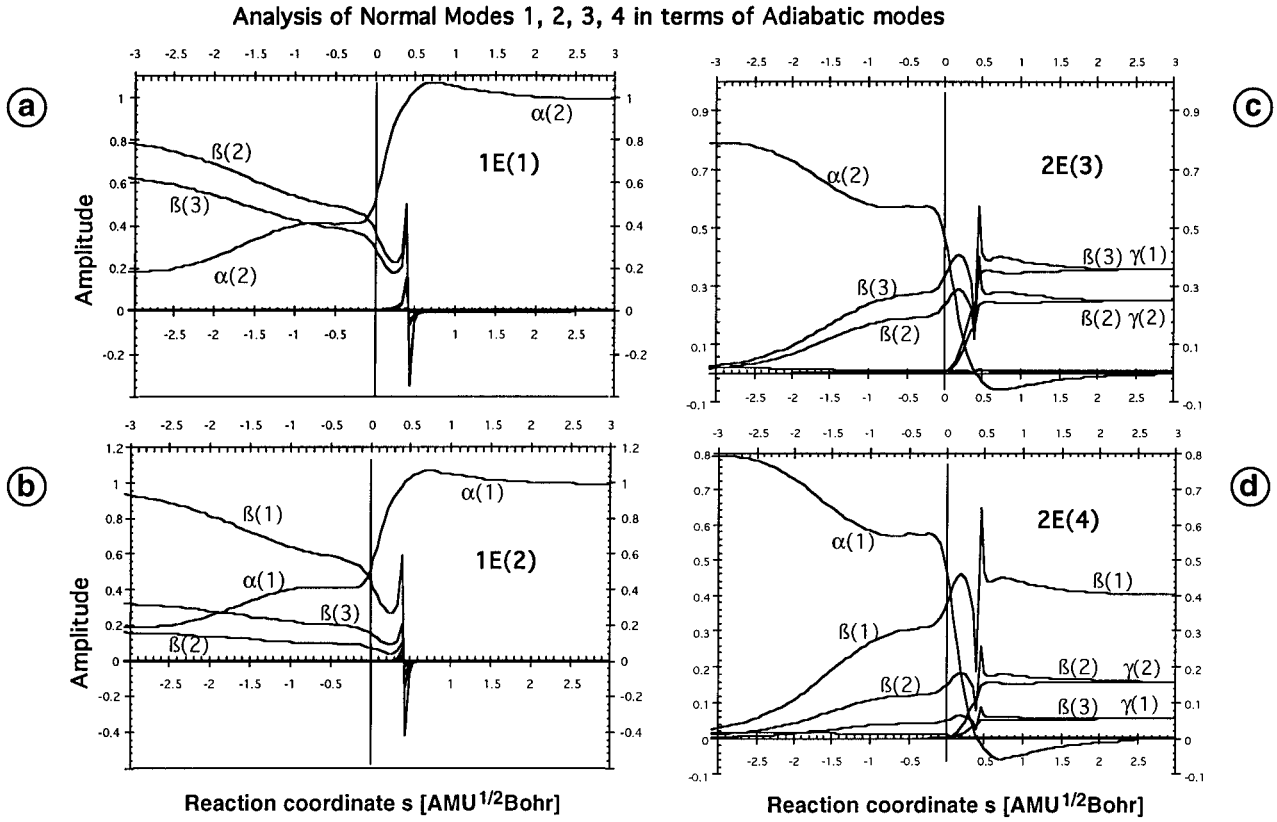

Figure 13. Characterization of the 1e (a and b) and 2e symmetric modes (c and d) in terms of generalized adiabatic modes. For a definition of parameters, compare with Scheme 2. The position of the transition state corresponds to $s = 0$ amu$^{1/2}$ a_0 and is indicated by a vertical line.

breakage. Apart from this, it has to be considered that the investigation of the *van der Waals region on the product side* is carried out from some distant position on the energy ridge between the three reaction valleys to the right of the bifurcation point so that a small but distinct curvature peak in this region might be lost.

Characterization of all normal modes in terms of generalized adiabatic modes also leads to an identification of those vibrational modes which are converted into rotations or translations. Table 2 gives a summary of all results, which reveal that in the course of the reaction two rotations of CH_3 and two rotations of H_2 are converted into the 1e and 2e vibrations of the reaction complex, of which the 1e vibrations become rotations of CH_4. Figure 13 gives the characterization of the 1e and 2e modes in terms of generalized adiabatic modes, which provide the basis of the analysis. The 1e modes obtain increasing β character for decreasing s, while the α contribution decreases to zero for s toward $-\infty$. The angles β describe the rotation of CH_3 at the two axes perpendicular to the C_3 axis of the $CH_3\cdots H_2$ complex. For increasing s (to the right of the TS), the character of the 1e modes is totally determined by the α-component also describing rotation of CH_4 at the two axes perpendicular to the C_3 axis of the $CH_3\cdots H_2$ complex. In the case of degenerate modes 2e, α-rotations of a noninteracting H_2 (strongly negative s) are converted into β bending vibrations of CH_4 (strongly positive s) as can be seen by inspection of Figure 13. Hence, the adiabatic mode analysis provides an exact account of vibrational, rotational, and translational modes during the reaction.

If one considers just the energy profile of Figure 1 and the geometry diagram of Figure 2, reaction I has a rather simple mechanism characterized just by a simultaneous breaking of the HH and forming of the CH bond. However, in Figures 1 and 2 details are hidden that can be unravelled by URVA. This is made transparent in Figure 14 for the changes in R2 as described by R2(s), which are amplified in a schematic way with the help of the reaction path curvature $\kappa(s)$ so that features can be seen that are difficult to see in Figure 2. The function R2(s) can be dissected in five different phases in which the reduction of the distance R2 to a CH bond length of CH_4 is accelerated or slowed down. The inflection points i_1, i_2, and i_3 of R2(s) (Figures 2 and 14) are the centers of the acceleration and slowing down regions. They are easily determined by the positions of $A_{n,s}{}^{\kappa}[\mathrm{R2}] = A_{n,s}[\mathrm{R2}] = 0$ (Figure 8b), while the borders of these regions are given by the curvature peaks $\kappa 1$, $\kappa 2$, and $\kappa 3$ (Figures 8 and 14). In the reactant region ($s < -2.5$ amu$^{1/2}$ a_0), the reaction complex resists a decrease of R2 because this increases exchange repulsion between the reactants and an increase of the total energy. At curvature peak $\kappa 1$ ($s = -2.5$), pyramidalization of CH_3 starts (see also β in Figure 2), which within a short range ($-2.5 < s < -2.1$) leads to some significant changes in the electronic structure due to the conversion of a π- to a σ-radical. This is accompanied by an accelerated decrease of R2 (increase of $A_{n,s}{}^{\kappa}[\mathrm{R2}]$) and the first coupling of the R2 coordinate with the reaction coordinate as revealed by a large value of $k_a[\mathrm{R2}]$ at -2.2 amu$^{1/2}$ a_0.

Once pyramidalization has been initiated, any further decrease of R2 has to be supported by polarization of H2 and additional pyramidalization of CH_3, which is difficult due to an increase in exchange repulsion (maximum of the R2 force at $s = -0.5$ amu$^{1/2}$ a_0). Accordingly, the decrease of R2 is slowed down in the region $-2.1 < s < -0.2$ accompanied by a decrease of the amplitude $A_{n,s}{}^{\kappa}[\mathrm{R2}]$, which reaches its minimum at $s = -0.2$ (Figure 14). Hence, the preparation region is characterized by a short initialization region of pyramidalization (indicated by the maximum of $k_a[\mathrm{R2}]$: first coupling of R2 with reaction coordinate) and a broad pyramidalization−polarization region characterized by the repulsive maximum in the R2 force.

Once the HH bond starts to split, there is another acceleration phase of R2 ($-0.2 < s < 0.65$) to form the CH bond mainly due to the inductive attraction between CH_3 and H_2 (R2 force

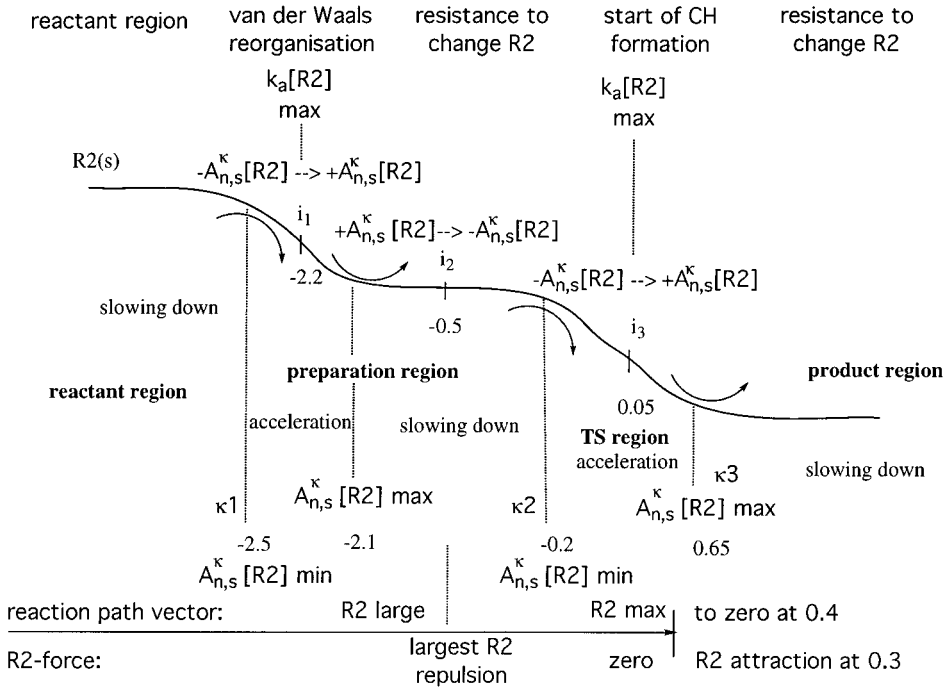

Figure 14. Schematic representations of details of the curve R2(*s*) shown in Figure 2. Inflection points i_j and the curvature of R2(*s*) are indicated and used to differentiate between regions of acceleration and slowing down of the reduction of R2 to the CH bond length of CH_4. Positions *s* (in amu$^{1/2}$ a_0) are taken from the curvature diagram (Figure 8b), the adiabatic force constant diagram (Figure 6), the reaction path vector analysis (Figure 3), and the diagram of the forces (Figure 4). See text.

is zero at TS and becomes negative for larger *s*). The second coupling between R2 and reaction coordinate occurs as indicated by the maximum of k_a[R2] at the TS and the maximum of the R2 component of $\boldsymbol{\eta}(s)$ (Figure 14). The inclusion of the R2 force into the discussion is justified because the reaction path vector $\boldsymbol{\eta}(s)$ is dominated by R2 up to the point $s = 0.4$ amu$^{1/2}$ a_0. Beyond this point, the R1 component dominates, and therefore, the R1 force has to be considered.

Figure 14 clearly demonstrates that $q_n(s)$ (Figure 2), $\boldsymbol{\eta}(s)[q_n]$ (Figure 3), and $\kappa(s)[q_n]$ (Figure 8) are closely related in the sense that the latter quantities provide the fine and hyperfine analysis of the geometry changes accompanying the reaction (Figure 2). Different phases in the changes of q_n can be distinguished that are centered at the positions of maximal change in the adiabatic force constant and the internal force associated with q_n. The latter are related to the energy profile and the changes in the electron density distribution (Figure 11) so that a complete picture of the reaction mechanism emerges.

6. Conclusions

In this work, we have presented the URVA as a new unified method to investigate reaction mechanism. URVA is based on the concept of the RPH and the concept of a generalized characterization of normal modes (CNM) described previously.[8,9] In particular, it combines the analysis of properties that were previously only separately or not at all investigated in connection with the RPH approach:

(a) *Characterization of normal vibrational modes, reaction path vector* $\boldsymbol{\eta}(s)$*, and curvature vector* $\kappa(s)$ *in terms of generalized adiabatic modes associated with internal parameters* ζ_n *(or internal coordinates* q_n*) used to describe the reaction complex.* Essential for this description is the derivation of a generalized amplitude $A_{\mu,n}(s)$ (related to coupling coefficients $B_{\mu,s}(s)$ and $B_{\mu,\nu}(s)$) for $\boldsymbol{\eta}(s)$ and $\kappa(s)$, which is independent of the composition of the internal parameter set and complies with the symmetry of the reaction complex.

(b) *An analysis of electronic structure changes in dependence of s in terms of attractive and repulsive internal forces, changes in the electron density distribution, and its associated Laplace concentration.* Essential for the analysis of $\rho(\mathbf{r},s)$ is that response densities are used with proper corrections for basis set superposition errors and that a general reference density distribution is defined that makes it possible to calculate the difference density $\Delta\rho(\mathbf{r},s)$. Difference density distribution and Laplace concentration (not discussed here) provide direct insight into exchange repulsion and inductive attraction between reacting molecules.

The strength of the URVA approach is that different properties such as energies, geometries, internal forces, electron density distribution, vibrational modes, reaction path vector, or curvature vector are analyzed using one and the same set of internal parameters that is chosen to comply with the language of chemists (e.g. by using internal coordinates as internal parameters). URVA is a direct method, which means that all needed calculations are done in one step once reactant, product, and TS energies and geometries are determined.

URVA has been applied to the hydrogenation reaction of the methyl radical leading to a number of important conclusions concerning the mechanism of this reaction, which were previously not determined.

(1) Five different phases of the reaction can be distinguished: (a) reactant phase, (b) van der Waals phase on the reactant side, preparation phase, (c) TS phase, (d) van der Waals phase on the product side, finalization phase, and (e) product phase.

(2) The TS region is limited by large curvature peaks that are typical of bond formation or bond cleavage. In the case of reaction I, the TS region stretches from $s = -0.2$ to $s = 0.65$ amu$^{1/2}$ a_0; i.e. the center of the TS region does not coincide with the position of the TS. The latter is shifted by $\Delta s = 0.3$ amu$^{1/2}$ a_0 into the entrance channel of reaction I indicative of an early TS.

(3) By the relative heights and the positions of the curvature peaks in the TS region, the diagram of $\kappa(s)$ reveals that reaction I is exothermic and that an early TS is encountered. Hence, the contents of the Hammond postulate can be quantified by investigation of the diagram $\kappa(s)$.

(4) Van der Waals complexes occupy local minima of a PES at distances larger than typical bond distances. If, however, attractive and repulsive forces of a van der Waals complex compensate each other, there is no possibility to detect experimentally electronic structure changes of reacting molecules that are typical of van der Waals complexes. The detection of the small curvature peak $\kappa 1$ in the entrance channel of reaction I (previously not found[13−20]) confirms that at $s = -2.5$ amu$^{1/2}$ a_0) electronic structure changes typical of a van der Waals complex occur. The van der Waals complex actually is not formed since exchange repulsion is always larger than inductive attraction between CH_3 and H_2. However, it is justified to speak of the van der Waals phase of reaction I.

(5) The van der Waals phase splits into a small region, in which pyramidalization of planar CH_3 is initialized, and a larger region, in which additional pyramidalization and polarization of both CH_3 and H_2 accompany a decrease of the distance R2 between the reactants. In these regions, the reactants are prepared for the reaction (preparation region), which requires energy since exchange repulsion reaches a maximum (indicated by the force connected with R2). After the maximum, inductive attraction compensates exchange repulsion more and more and leads the reaction into the TS region.

(6) There are two "acceleration phases" along the reaction path, in which the approach between the reactants is supported by appropriate electronic structure changes. One of them is located at the beginning of the reactant preparation phase and corresponds to the initialization of pyramidalization, while the other is at the beginning of the TS region and corresponds to the start of HH bond cleavage. Acceleration of the approach between the reactants leads to a coupling of the approach parameter R2 with the reaction coordinate, which is indicated by large maxima in the generalized adiabatic force constant k_a[R2].

(7) The product preparation region is indicated in the diagram $\kappa(s)$ by just a shoulder in the CH bond formation peak. This is due to two reasons: (a) an approaching H atom does not cause typical van der Waals changes in the electronic structure of CH_4 at distances larger than 1.5 Å since its polarizing capacity is too small; (b) a bifurcation point at $s = 0.4$ amu$^{1/2}$ a_0 hinders an exact investigation of the exit channel of the reaction.

Application of URVA to more complicated reactions has shown already that the mechanistic features found for reaction I can generally be observed in these cases. There is indication that URVA leads to a better understanding of reaction mechanism.[35]

Acknowledgment. This work was supported by the Swedish Natural Science Research Council (NFR). All calculations were done on the CRAY YMP/416 of the Nationellt Superdatorcentrum (NSC), Linköping, Sweden. The authors thank the NSC for a generous allotment of computer time. Useful comments by Tobias Johnsson are appreciated.

References and Notes

(1) Miller, W. H.; Handy, N. C.; Adams, J. E. *J. Chem. Phys.* **1980**, *72*, 99.

(2) (a) Fukui, K. *J. Phys. Chem.* **1970**, *74*, 4161. (b) Fukui, K. *Acc. Chem. Res.* **1981**, *14*, 363.

(3) Page, M.; McIver, J. W. J. *J. Chem. Phys.* **1988**, *88*, 922.

(4) Kato, S.; Morokuma, K. *J. Chem. Phys.* **1980**, *73*, 3900.

(5) For reviews, see: (a) Morokuma, K.; Kato, S. In *Potential energy characteristics for chemical reactions*; Truhlar, D. H., Ed.; Plenum: New York, 1981; p 243. (b) Miller, W. In *The Theory of Chemical Reaction Dynamics*; Clar, D. C., Ed.; Reidel: Dordrecht, 1986; p 27. (c) Truhlar, D.; Garrett, B. *Annu. Rev. Phys. Chem.* **1986**, *35*, 159. (d) Truhlar, D.; Steckler, R.; Gordon, M. *Chem. Rev.* **1987**, *87*, 217. (e) Truhlar, D.; Brown, F. Steckler, R.; Isaacson, A. In *The Theory of Chemical Reaction Dynamics*; Clar, D. C., Ed.; Reidel: Dordrecht, 1986; p 285.

(6) Kraka, E.; Dunning, T. H. In *Advances in Molecular Electronic Structure Theory: The Calculation and Characterization of Molecular Potential Energy Surfaces*; Dunning, T. H., Ed.; JAI Press, Inc.: Greenwich, CT, 1990; p 129.

(7) Konkoli, Z.; Cremer, D. Submitted for publication in *J. Chem. Phys*.

(8) Konkoli, Z.; Larsson, A.; Cremer, D. Submitted for publication in *J. Chem. Phys*.

(9) Konkoli, Z.; Cremer, D. Submitted for publication in *J. Chem. Phys.*

(10) Konkoli, Z.; Larsson, A.; Cremer, D. Submitted for publication in *J. Chem. Phys*.

(11) For reviews, see: (a) Shaw, R. *J. Phys. Chem. Ref. Data* **1978**, *7*, 1179. (b) Allara, D. L.; Shaw, R. *J. Phys. Chem. Ref. Data* **1980**, *9*, 523. (c) Tsang, W.; Hampson, R. F. *J. Phys. Chem. Ref. Data* **1986**, *15*, 1087. For recent work, see: (d) Knyazev, V. D.; Bencsura, A.; Stoliarov, S. I.; Slagle, I. R. *J. Phys. Chem.* **1996**, *100*, 11346. (e) Baeck, H. J.; Shin, K. S.; Yang, H.; Qin, Z.; Lissianski, V.; Gardiner, W. C. *J. Phys. Chem.* **1995**, *99*, 15925. (f) Rabinowitz, M. J.; Sutherland, J. W.; Patterson, P. M.; Klemm, R. B. *J. Phys. Chem.* **1991**, *95*, 674. (g) Zhang, H. X.; Back, M. H. *Int. J. Chem. Kinet.* **1990**, *22*, 21.

(12) Kraka, E.; Gauss, J.; Cremer, D. *J. Chem. Phys.* **1993**, *99*, 5306 and references cited therein.

(13) Yamashita, K.; Yamabe, T. *Int. J. Quantum Chem., Symp.* **1983**, *17*, 177.

(14) Schatz, G. C.; Wagner, A. F.; Dunning, T. H. *J. Phys. Chem.* **1984**, *88*, 221.

(15) Boatz, J. A.; Gordon, M. S. *J. Phys. Chem.* **1989**, *93*, 5774.

(16) Baldridge, K. K.; Gordon, M. S.; Steckler, R.; Truhlar, D. G. *J. Phys. Chem.* **1989**, *93*, 5107.

(17) Truong, T. N. *J. Chem. Phys.* **1994**, *100*, 8014.

(18) Truong, T. N.; Duncan, W. J. *J. Chem. Phys*. **1994**, *101*, 7408.

(19) Taketsugu, T.; Gordon, M. S. *J. Chem. Phys.* **1996**, *104*, 2834.

(20) (a) Tachibana, A.; Hori, K.; Asai, Y.; Yamabe, T.; Fukui, K. *THEOCHEM* **1985**, *123*, 267. (b) Steckler, R.; Dykema, K. J.; Brown, F. B.; Hancock, G. C.; Truhlar, D. G.; Valencich, T. *J. Chem. Phys.* **1987**, *87*, 7024. (c) Joseph, T.; Steckler, R.; Truhlar, D. G. *J. Chem. Phys*. **1987**, *87*, 7036. (d) Garrett, B. C.; Redmon, M. J.; Steckler, R.; Truhlar, D. G.; Baldridge, K. K.; Bartol, D.; Schmidt, M. W.; Gordon, M. S. *J. Phys. Chem.* **1988**, *92*, 1476. (e) Sironi, M.; Cooper, D. L.; Gerratt, J.; Raimondi, M. *J. Am. Chem. Soc.* **1990**, *112*, 5054. (f) Furue, H.; Pacey, P. D. *J. Phys. Chem.* **1990**, *94*, 1419. (g) Natanson, G. A.; Garrett, B. C.; Truong, T. N.; Joseph, T.; Truhlar, D. G. *J. Chem. Phys.* **1991**, *94*, 7875. (h) Gonzales, U. A.; Menedez, M.; Sole, S. A.; Aguilar, N. A. *Chem. Phys. Lett*. **1991**, *176*, 315. (i) Gonzales, L. A.; Truong, T. N.; Truhlar, D. G. *J. Chem. Phys.* **1991**, *95*, 8875. (j) Melissas, V. S.; Truhlar, D. G.; Garrett, B. C. *J. Chem. Phys.* **1992**, *96*, 5758. (k) Lu, D. H.; Truhlar, D. G. *J. Chem. Phys.* **1993**, *99*, 2723. (l) Jackels, C. F.; Gu, Z.; Truhlar, D. G. *J. Chem. Phys.* **1995**, *102*, 3188. (m) Jordan, M. J. T.; Gilbert, R. G. *J. Chem. Phys.* **1995**, *102*, 5669. (n) Takayanagi, T. *J. Chem. Phys.* **1996**, *104*, 2237.

(21) Pulay, P.; Fogarasi, G. *J. Chem. Phys.* **1992**, *96*, 2856.

(22) Cremer, D.; Pople, J. A. *J. Am. Chem. Soc*. **1975**, *97*, 1354.

(23) Morino, Y.; Kuchitsu, K. *J. Chem. Phys.* **1952**, *20*, 1809.

(24) (a) Pulay, P.; Török, F. *Acta Chim. Hung.* **1966**, *47*, 273. (b) Keresztury, G.; Jalsovszky, G. *J. Mol. Struct.* **1971**, *10*, 304.

(25) (a) Møller, C.; Plesset, M. S. *Phys. Rev.* **1934**, *46*, 618. (b) Binkley, J. S.; Pople, J. A. *Int. J. Quantum Chem.* **1975**, *9*, 229.

(26) Hariharan, P. C.; Pople, J. A. *Theor. Chim. Acta* **1973**, *28*, 213.

(27) Gonzales, C.; Schlegel, B. H. *J. Chem. Phys.* **1989**, *90*, 2154. (b) Gonzales, C.; Schlegel, B. H. *J. Phys. Chem.* **1990**, *94*, 5523.

(28) Konkoli, Z.; Cremer, D. Submitted for publication in *J. Comput. Chem.*

(29) Boys, F.; Bernardi, F. *Mol. Phys.* **1970**, *19*, 553.

(30) Kraka, E.; Cremer, D.; Spoerel, U.; Merke, I.; Stahl, W.; Dreizler. *J. Phys. Chem.* **1995**, *99*, 12466.

(31) Konkoli, Z.; Cremer, D. ADIA, A FORTRAN Program for the Adiabatic Mode Analysis and the Unified Reaction Path Analysis, Göteborg, Sweden, 1996.

(32) Kraka, E.; Gauss, J.; Reichel, F.; Olsson, L.; He, Z.; Konkoli, Z.; Cremer, D. COLOGNE96, Göteborg, Sweden, 1996.

(33) Frisch, M. J.; Trucks, G. W.; Schlegel, H. B.; Gill, P. M. W.; Johnson, B. G.; Robb, M. A.; Cheeseman, J. R.; Keith, T.; Petersson, G. A.; Montgomery, J. A.; Raghavachari, K.; Al-Laham, M. A.; Zakrzewski, V. G.; Ortiz, J. V.; Foresman, J. B.; Cioslowski, J.; Stefanov, B. B.; Nanayakkara, A.; Challacombe, M.; Peng, C. Y.; Ayala, P. Y.; Chen, W.; Wong, M. W.; Andres, J. L.; Replogle, E. S.; Gomperts, R.; Martin, R. L.; Fox, D. J.; Binkley, J. S.; Defrees, D. J.; Baker, J.; Stewart, J. P.; Head-Gordon, M.; Gonzalez, C.; Pople, J. A. *GAUSSIAN 94*; Gaussian Inc.: Pittsburgh, PA, 1995.

(34) (a) Morse, P. M.; Feshbach, H. *Methods of Theoretical Physics*; McGraw-Hill, New York, 1953; Vol. 1, p 6. (b) Kraka, E.; Cremer, D. In *Theoretical Models of Chemical Bonding*; Maksic, Z. B., Ed.; Springer: Berlin, 1990; Vol. 2, p 453.

(35) Johnsson, T.; Konkoli, Z.; Kraka, E.; Cremer, D. To be published.